Cell Reports
Medicine

Article

Cholesterol 24-hydroxylase at the choroid plexus contributes to brain immune homeostasis

Graphical abstract

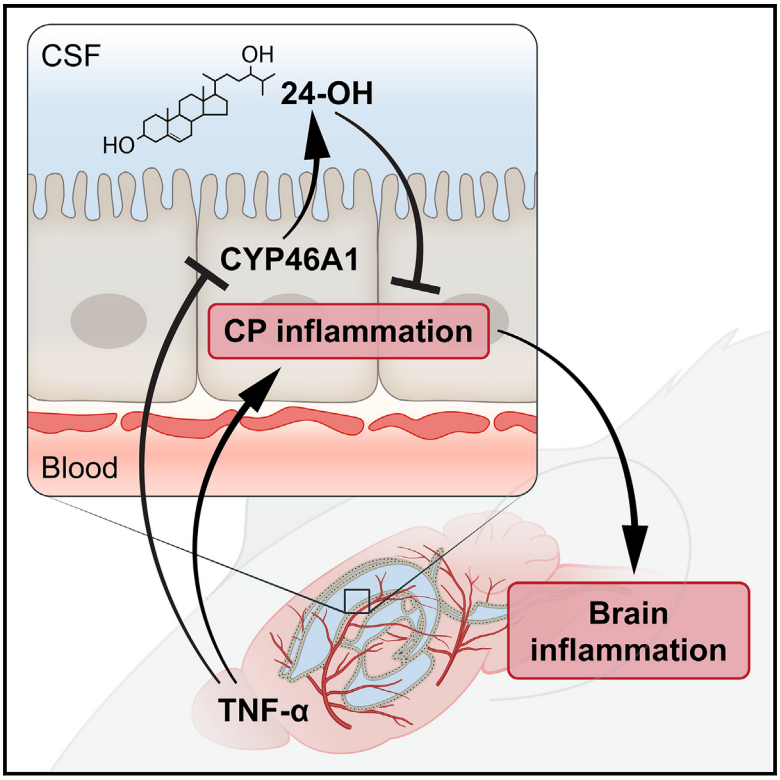

Authors

Afroditi Tsitsou-Kampeli, Stefano Suzzi, Mor Kenigsbuch, ..., Yosef Shaul, Ido Amit, Michal Schwartz

Correspondence

afroditi.tsitsou-kampeli@weizmann.ac.il (A.T.-K.), stefano.suzzi@pasteur.fr (S.S.), michal.schwartz@weizmann.ac.il (M.S.)

In brief

CYP46A1 is an enzyme that breaks down cholesterol in neurons. Tsitsou-Kampeli, Suzzi et al. demonstrate the choroid plexus as an additional, non-neuronal site for CYP46A1 expression in the brain. They further show that the CYP46A1 product, 24-OH, downregulates inflammatory programs in the choroid plexus, previously found to trigger brain dysfunction remotely.

Highlights

- The brain-specific enzyme CYP46A1 is expressed in the brain's CP epithelium
- CYP46A1 levels in the CP are decreased under brain conditions in mice and humans
- 24-OH, a product of CYP46A1, decreased disease-associated CP inflammation *in vitro*
- Enhanced CYP46A1 levels or activity in the CP increased resilience to inflammation

Tsitsou-Kampeli et al., 2023, Cell Reports Medicine *4*, 101278
November 21, 2023
https://doi.org/10.1016/j.xcrm.2023.101278

CellPress

Cell Reports Medicine

CellPress
OPEN ACCESS

Article

Cholesterol 24-hydroxylase at the choroid plexus contributes to brain immune homeostasis

Afroditi Tsitsou-Kampeli,[1,8,*] Stefano Suzzi,[1,7,8,*] Mor Kenigsbuch,[1,2] Akisawa Satomi,[1,3] Romano Strobelt,[4] Oded Singer,[5] Ester Feldmesser,[5] Maitreyee Purnapatre,[1] Sarah Phoebeluc Colaiuta,[1] Eyal David,[2] Liora Cahalon,[1] Oliver Hahn,[6] Tony Wyss-Coray,[6] Yosef Shaul,[4] Ido Amit,[2] and Michal Schwartz[1,9,*]

[1]Department of Brain Sciences, Weizmann Institute of Science, Rehovot, Israel
[2]Department of Immunology, Weizmann Institute of Science, Rehovot, Israel
[3]Graduate School of Pharmaceutical Sciences, The University of Tokyo, Tokyo, Japan
[4]Department of Molecular Genetics, Weizmann Institute of Science, Rehovot, Israel
[5]Life Sciences Core Facilities, Weizmann Institute of Science, Rehovot, Israel
[6]Department of Neurology and Neurological Sciences, Stanford University School of Medicine, Stanford, CA, USA
[7]Present address: Institut Pasteur, Université Paris Cité, Perception & Action Unit, F-75015 Paris, France; CNRS UMR3571, 75015, Paris, France
[8]These authors contributed equally
[9]Lead contact
*Correspondence: afroditi.tsitsou-kampeli@weizmann.ac.il (A.T.-K.), stefano.suzzi@pasteur.fr (S.S.), michal.schwartz@weizmann.ac.il (M.S.)
https://doi.org/10.1016/j.xcrm.2023.101278

SUMMARY

The choroid plexus (CP) plays a key role in remotely controlling brain function in health, aging, and disease. Here, we report that CP epithelial cells express the brain-specific cholesterol 24-hydroxylase (CYP46A1) and that its levels are decreased under different mouse and human brain conditions, including amyloidosis, aging, and SARS-CoV-2 infection. Using primary mouse CP cell cultures, we demonstrate that the enzymatic product of CYP46A1, 24(*S*)-hydroxycholesterol, downregulates inflammatory transcriptomic signatures within the CP, found here to be elevated across multiple neurological conditions. *In vitro*, the pro-inflammatory cytokine tumor necrosis factor α (TNF-α) downregulates CYP46A1 expression, while overexpression of CYP46A1 or its pharmacological activation in mouse CP organ cultures increases resilience to TNF-α. *In vivo*, overexpression of CYP46A1 in the CP in transgenic mice with amyloidosis is associated with better cognitive performance and decreased brain inflammation. Our findings suggest that CYP46A1 expression in the CP impacts the role of this niche as a guardian of brain immune homeostasis.

INTRODUCTION

Chronic brain inflammation is a common hallmark in multiple neurological conditions. Cumulative evidence highlights the pivotal role of the brain's choroid plexus (CP) in affecting brain inflammation. The CP is a specialized structure within the brain ventricles, consisting of a tight epithelium surrounding a stroma filled with fenestrated capillaries and forming a barrier that separates the blood from the cerebrospinal fluid (CSF). Under physiological conditions, the CP produces CSF, neurotrophic factors, and other signaling and carrier molecules, acts as a molecular and cellular gateway, and provides an entry site for immune cells required for brain surveillance and repair.[1,2] However, in various neurological conditions including aging, neurodegeneration, and some viral infections such as SARS-CoV-2, the CP becomes an additional source of inflammatory signals that perpetuate the damage within the brain parenchyma.[3–9]

The anatomical integrity of the CP is dependent on the expression and functional role of liver X receptors (LXR) α and β.[10] LXRs are transcription factors that regulate critical biological processes, primarily cholesterol homeostasis, but also immune and inflammatory responses.[11] LXRs are activated by endogenous cholesterol derivatives called oxysterols, synthesized by cholesterol hydroxylase enzymes.[12] It is conceivable that LXR signaling in the CP depends on oxysterol production by cholesterol hydroxylases expressed by the CP itself, based on the spatial separation of the CP from the brain parenchyma, and the fact that oxysterols act in an autocrine and paracrine manner.[13] One of the most potent LXR activators, and the most abundant oxysterol in the brain, is 24(*S*)-hydroxycholesterol (24-OH),[14–16] the product of the brain-specific enzyme cholesterol 24-hydroxylase (CYP46A1; see the Human Protein Atlas,[17] https://www.proteinatlas.org/ENSG00000036530-CYP46A1/tissue). CYP46A1 is the major enzyme involved in cholesterol elimination from the brain[18] and is primarily expressed by neurons under physiological conditions (see the adolescent mouse brain atlas,[19] http://mousebrain.org/adolescent/genesearch.html, query "Cyp46a1"). Indirect evidence suggests that the *Cyp46a1* gene is also expressed in the mouse CP during embryogenesis.[20] However, the expression and function of CYP46A1 in the adult CP have not been investigated. Previous research demonstrated that 24-OH can stimulate

cholesterol release in a conditionally immortalized rat CP epithelial cell line (TR-CSFB3), suggesting the involvement of 24-OH/LXR signaling in regulating CSF cholesterol levels.[21]

Here, we hypothesized that the expression of CYP46A1 in the CP could impact the brain's health via the activity of 24-OH on the CP itself. We found that CYP46A1 is expressed by CP epithelial cells in both mice and humans and that its levels are significantly decreased in different brain conditions. We further found that primary mouse CP cell cultures exposed to 24-OH downregulated inflammatory transcriptomic signatures. Upon reanalyzing publicly available transcriptomic datasets, we observed consistent expression of these signatures in the CP of mice and humans under different brain conditions. Moreover, we demonstrated *in vitro* that CYP46A1 expression in CP cells was negatively affected by the pro-inflammatory cytokine tumor necrosis factor α (TNF-α), whereas CYP46A1 overexpression or its pharmacological activation in mouse CP organ cultures increased resilience to TNF-α challenge. Finally, CYP46A1 overexpression via gene delivery in the CP in a mouse model of amyloidosis (5xFAD) was associated with protection of cognitive performance and attenuation of brain inflammation.

RESULTS

CYP46A1 in the CP is expressed by CP epithelial cells

We first demonstrated by immunohistochemistry (IHC) that CYP46A1 protein is expressed by CP epithelial cells in both mice and humans (Figures 1A and 1B, respectively). We also used public single-nucleus transcriptomic data from mouse[22] (Figures 1C–1G) and human[3] (Figures 1H–1J). In the mouse we found that, among the different CP cell types, *Cyp46a1* is expressed predominantly in epithelial cells (Figures 1C, 1D, and 1G). In addition, we found that *Cyp46a1* is expressed in both young (4 months old) and aged mice (20 months old) (Figures 1C and 1E), and in all four brain ventricles (Figures 1C and 1F). In the human we found that *CYP46A1* is expressed predominantly in epithelial cells (Figures 1H–1J) and confirmed that both mouse and human CP epithelial cells express the genes *Nr1h2/NR1H2*, encoding LXR-β, and *Nr1h3/NR1H3*, encoding LXR-α (Figures 1K and 1L).

Comparing the expression of mouse *Cyp46a1* and human *CYP46A1* to that of other cholesterol hydroxylase genes,[12,23] namely cholesterol 25-hydroxylase (*Ch25h/CH25H*), cholesterol 7α -hydroxylase (*Cyp7a1/CYP7A1*), cholesterol 20-22-desmolase (*Cyp11a1/CYP11A1*), and cholesterol 27-hydroxylase (*Cyp27a1/CYP27A1*), revealed that CP epithelial cells mostly express *Cyp46a1/CYP46A1* and *Cyp27a1/CYP27A1*, with *Cyp46a1* transcripts being more prevalent in mice (Figure 1M) and *CYP27A1* being more abundantly expressed in humans (Figure 1N). Since 24-OH is a more potent LXR activator than 27-hydroxycholesterol, the enzymatic product of CYP27A1,[14,15] we considered that CYP46A1/24-OH is the functionally relevant cholesterol hydroxylase/oxysterol system in the CP of both mouse and human.

CYP46A1 expression in the CP is decreased under multiple brain conditions

The discovery that CYP46A1 is expressed by the CP prompted us to examine whether its expression is altered in the CP in conditions of brain inflammation and cognitive impairment, previously linked to CP dysfunction.[3–9] We first compared the expression of CYP46A1 in the CP between transgenic mice with amyloidosis (5xFAD) and age-matched wild-type (WT) mice at a disease stage when cognitive dysfunction is manifested[24] (9–12 months of age). We found that CYP46A1 in the CP of 5xFAD mice was decreased relative to the WT controls as assessed by qRT-PCR (Figure 2A), IHC (Figures 2B–2D), and western blot (Figures S1A–S1D). To rule out loss of CP epithelial cells as the cause for the decreased CYP46A1 expression, we measured by qRT-PCR the expression of *Cdh1*, encoding the epithelial adherent junction component E-cadherin (Figure 2E), and by IHC the levels of immunolabeled claudin-1, a tight junction protein of the CP (Figures 2F and 2G), and the cell death marker cleaved caspase-3 (Figures 2H and 2I). We found no difference between 5xFAD and WT mice in the expression of these markers (Figures 2E–2I), suggesting that the observed decrease in CYP46A1 in the CP is likely due to decreased enzyme expression per cell rather than loss of CP epithelial cells. Of note, at the same disease stage (12 months), no change in CYP46A1 protein levels was detected between 5xFAD and WT mice in either the hippocampus or the cortex, as assessed by western blot (Figures S1E–S1L). We then examined postmortem CP samples of human Alzheimer's disease (AD) patients relative to age-matched individuals with no clinical record of dementia (non-demented [ND]). Quantification of images of CYP46A1 immunostaining in CP epithelial cells revealed a significant decrease with aging in both AD and ND samples, with different effects depending on the disease status (Figures 2J and 2K). Advancing age was the most prominent variable associated with CYP46A1 loss in the analyzed samples (age range 72–103 for AD, 73–95 for ND; Table S1). We also examined how CYP46A1 expression changes during physiological aging in mice. To accomplish this, we analyzed bulk transcriptome data of the WT mouse brain across the lifespan (provided by Hahn et al.[25]). We found decreased *Cyp46a1* gene expression in the CP in middle-aged mice (12–15 months relative to 3 months; Figure 2L). In addition, assessment of *Cyp46a1* expression in the other brain areas (Figures S2A–S2N) revealed a decrease in the motor cortex, albeit at a later time point (18–28 months relative to 3 months; Figure S2F). Given the frequent reports of cognitive deficits in individuals who had successfully recovered from SARS-CoV-2 virus infection,[26,27] we also examined the impact of COVID-19 (COVID) on CYP46A1 in the CP by analyzing the recently published[3] single-nucleus transcriptome data of postmortem CP samples from individuals who succumbed to COVID versus non-infected controls. Of note, the postmortem brain cortices of the same COVID patients exhibited neurodegeneration-associated transcriptomic signatures in the absence of traces of SARS-CoV-2 virus.[3] Analysis of *CYP46A1* gene expression per cell across samples revealed that COVID was linked to a slight decrease in CP epithelial cells ($\log_2$ fold change [$\log_2$fc] = −0.029; Figure 2M), although the difference did not pass multiple testing correction (non-adjusted MAST test, p = 0.009; false discovery rate [FDR]-adjusted p = 1.000). In the brain cortices, *CYP46A1* gene expression was modestly decreased in neurons (excitatory neurons: $\log_2$fc = −0.046; inhibitory neurons: $\log_2$fc = −0.064; neurogranin (NRGN)-positive neurons: $\log_2$fc = −0.080; Figure S2O) but increased in astrocytes ($\log_2$fc = 0.143;

CellPress
OPEN ACCESS

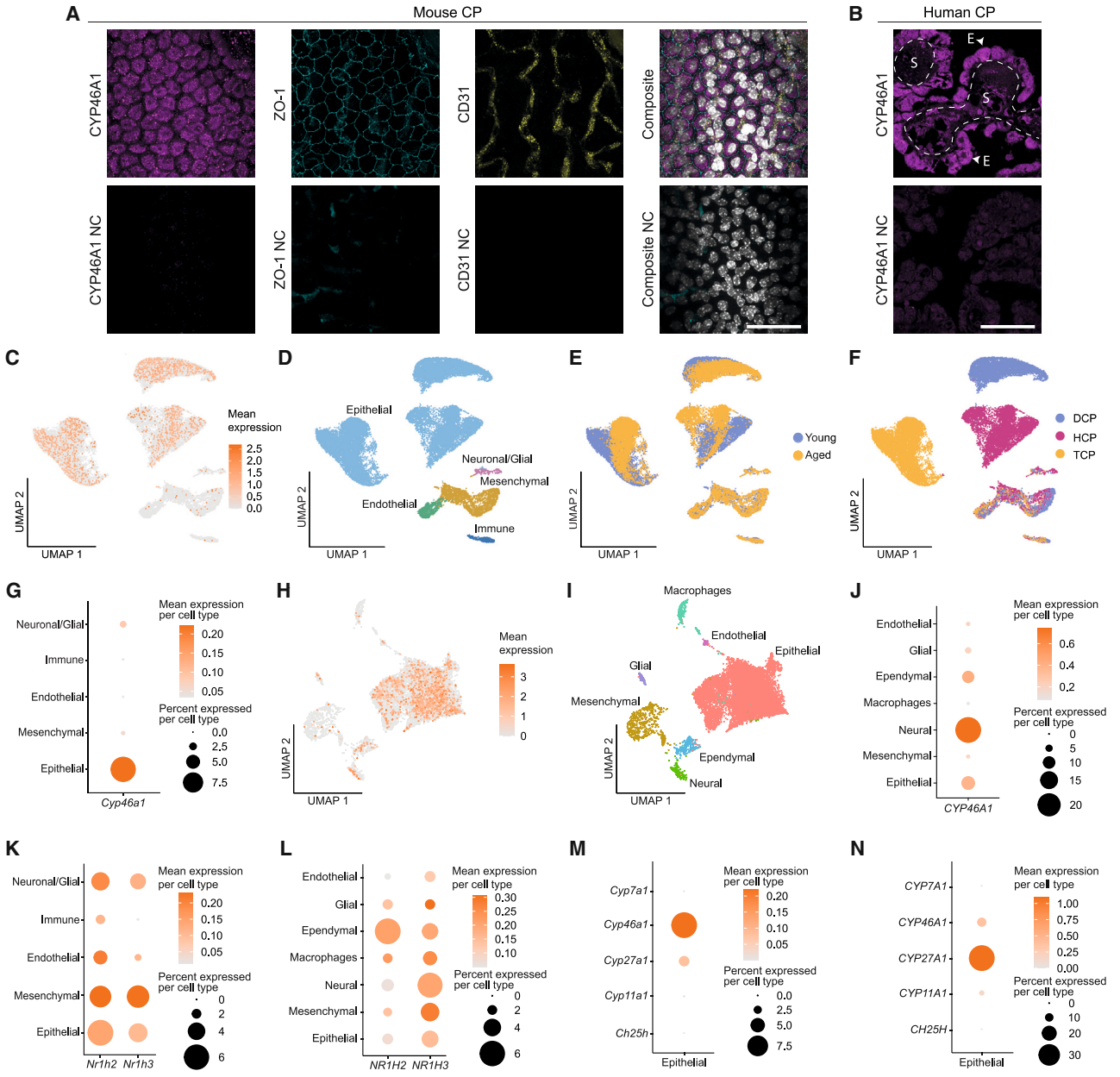

Figure 1. CP epithelial cells express CYP46A1 in mice and humans

(A and B) Representative images of whole-mount mouse CP (maximum-intensity projections; A) and sectioned human CP (B). Composite images show Hoechst-counterstained cell nuclei in white. NC, negative control with secondary antibody only. (A) ZO-1 stains for epithelial tight junctions, CD31 stains for blood vessels. (B) E, CP cuboidal epithelial cells; S, CP stroma. Scale bars, 50 μm.

(C–F) Uniform manifold approximation and projection (UMAP) embedding of single-nucleus profiles showing the cellular landscape of the adult mouse CP. Data retrieved from Dani et al.[22] (C) Distribution of mouse *Cyp46a1* gene expression (log_2(TP10K+1)) in the CP cellular landscape. (D–F) Colored annotations showing mouse CP cell types (D), mouse age groups (young = 4 months, aged = 20 months; E), and ventricle origin of the analyzed CP cells (F). DCP, diencephalic CP; HCP, hindbrain CP; TCP, telencephalic CP.

(G) Dot plot representing mouse *Cyp46a1* expression (log_2(TP10K+1)) across CP cell types.

(H and I) UMAP embedding of single-nucleus profiles showing the cellular landscape of the human CP. Data retrieved from Yang et al.[3] (H) Distribution of human *CYP46A1* gene expression (natural log of normalized counts) in the CP cellular landscape. (I) Colored annotations showing human CP cell types.

(J) Dot plot representing human *CYP46A1* expression across CP cell types (natural log of normalized counts).

(K) Dot plot representing the expression of mouse *Nr1h2* and *Nr1h3* genes (log_2(TP10K+1)) across CP cell types.

(L) Dot plot featuring the expression of human *NR1H2* and *NR1H3* genes (natural log of normalized counts) across CP cell types.

(M) Dot plot representing the expression of mouse *Cyp46a1* and other cholesterol hydroxylase genes (log_2(TP10K+1)) in CP epithelial cells.

(N) Dot plot representing the expression of human *CYP46A1* and other cholesterol hydroxylase genes (natural log of normalized counts) in CP epithelial cells.

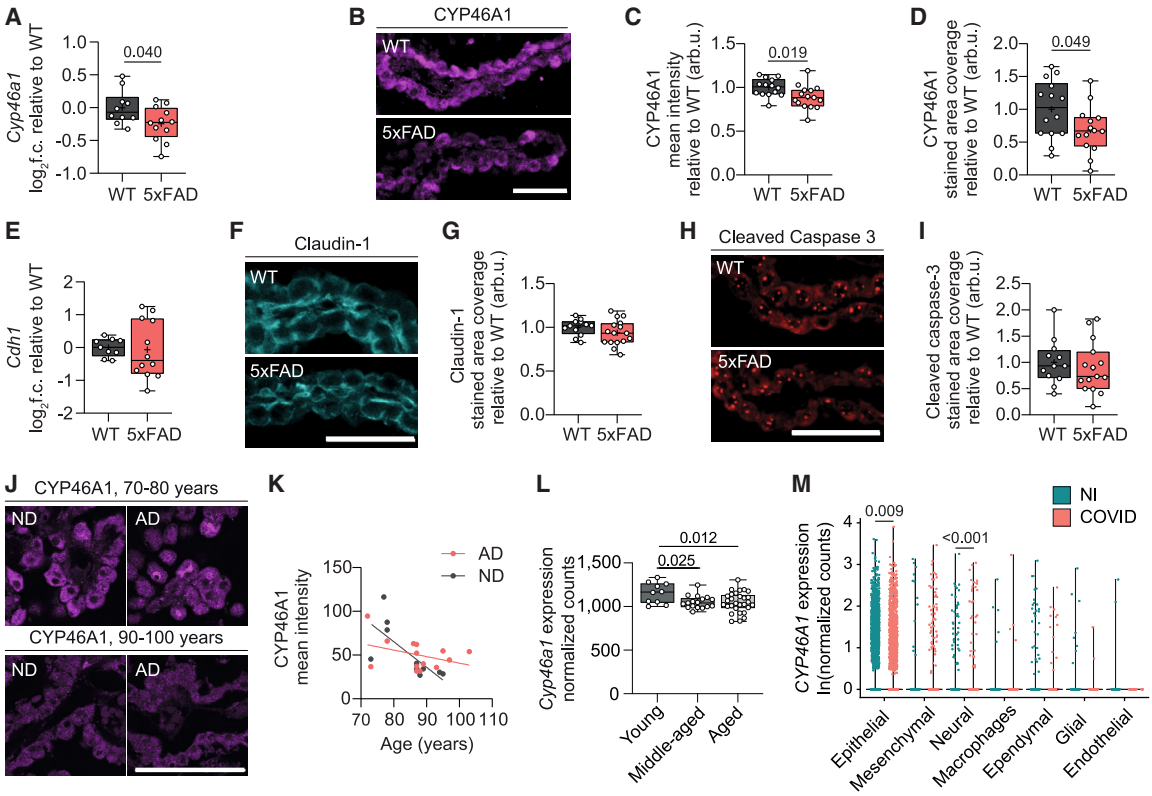

Figure 2. CYP46A1 expression in the CP is decreased across multiple brain conditions in mice and humans

(A) *Cyp46a1* gene expression in the CP in 5xFAD mice of 12 months relative to age-matched WT controls, measured by qRT-PCR. Sample numbers of mice: WT, n = 10; 5xFAD, n = 12. Statistical analysis: two-tailed unpaired Student's t test.

(B–D) CYP46A1 protein levels in the CP in 5xFAD mice of 9–12 months relative to age-matched WT controls, measured upon IHC. See also Figure S1. (B) Representative images. Scale bar, 50 μm. (C and D) Quantification of CYP46A1 levels as mean signal intensity of stained area (C) and stained area coverage over total CP area (D); arb. u., arbitrary units. Merged results from two experiments. Sample numbers of mice: (C) WT, n = 14; 5xFAD, n = 15; (D) WT, n = 14, 5xFAD, n = 14. Statistical analysis: two-tailed unpaired Student's t test.

(E) *Cdh1* gene expression in the CP in 5xFAD mice of 12 months relative to age-matched WT controls, measured by qRT-PCR. Sample numbers of mice: WT, n = 9; 5xFAD, n = 12. Statistical analysis: two-tailed unpaired Student's t test with Welch's correction.

(F and G) Claudin-1 protein levels in the CP in 5xFAD mice of 9–12 months relative to age-matched WT controls, measured upon IHC. (F) Representative images. Scale bar, 50 μm. (G) Quantification of claudin-1 levels as stained area coverage over total CP area; arb. u., arbitrary units. Merged results from two experiments. Sample numbers of mice: WT, n = 12; 5xFAD, n = 16. Statistical analysis: two-tailed unpaired Student's t test.

(H and I) Cleaved caspase-3 protein levels in the CP in 5xFAD mice of 9–12 months relative to age-matched WT controls, measured upon IHC. (H) Representative images. Scale bar, 50 μm. (I) Quantification of cleaved caspase-3 levels as stained area coverage over total CP area; arb. u., arbitrary units. Merged results from two experiments. Sample numbers of mice: WT, n = 12; 5xFAD, n = 15. Statistical analysis: two-tailed unpaired Student's t test.

(J and K) CYP46A1 protein levels in the CP in postmortem samples from human AD patients and ND controls, measured upon IHC. (J) Representative images. Scale bar, 50 μm. (K) CYP46A1 levels, quantified as mean signal intensity of stained area, as a function of age. Linear regression lines for AD (red line) and ND samples (black line) are shown separately. Sample numbers of human individuals: ND, n = 11; AD, n = 14. See also Table S1.

(L) *Cyp46a1* gene expression in the mouse CP across lifespan. Data provided by Hahn et al.[25] Young: 3 months; middle-aged: 12–15 months; aged: 18–28 months. Sample numbers of mice: young, n = 10; middle-aged, n = 17; aged, n = 29. Statistical analysis: one-way ANOVA followed by Dunnett's post hoc test comparing each group with the "young" group. See also Figures S2A–S2N.

(M) Violin plot showing human *CYP46A1* gene expression in the CP of COVID victims and age-matched non-infected controls (NI). Data retrieved from Yang et al.[3] The data from control individuals was the same as used for the analyses described in Figures 1H–1J, 1L, and 1N. See also Figure S2O. Statistical analysis: MAST test. The p values are not corrected for multiple testing.

In (A), (C–E), (G), (I), and (L), the box plots present the minimum and maximum values (whiskers), the first and third quartiles (box boundaries), the median (box internal line), and the mean (cross).

Figure S2O). Interestingly, decreased protein levels of neuronal CYP46A1 and concomitantly increased astrocytic CYP46A1 were previously observed in postmortem cortical samples from AD patients.[28] Overall, we found decreased CYP46A1 expression levels in the CP under different neurological conditions linked to cognitive deterioration.[3,4,6,26,27,29–34]

24-OH regulates genes associated with inflammation in CP epithelial cells

The above results led us to hypothesize that CYP46A1 might play a role in the lifelong maintenance of CP homeostasis via its product, 24-OH. To test the direct biological effect of 24-OH on the CP, we used primary mouse CP cell cultures, which are highly

CellPress
OPEN ACCESS

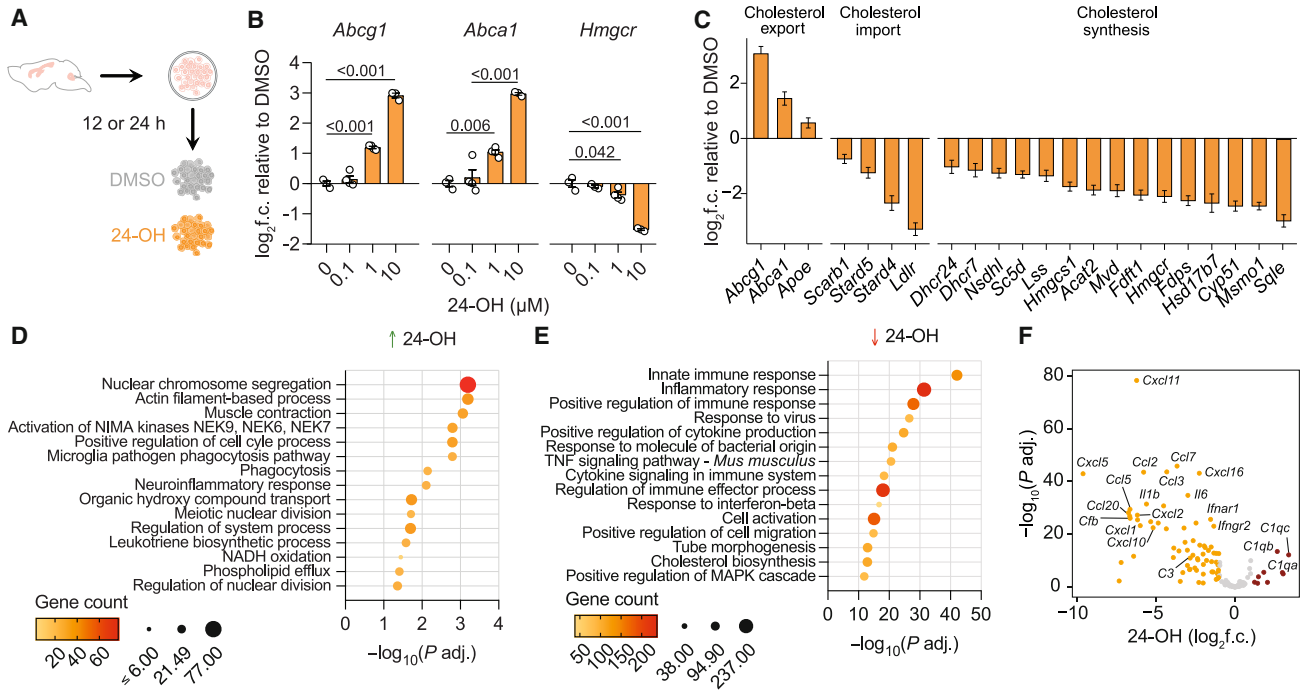

Figure 3. 24-OH negatively regulated inflammatory signatures in primary mouse CP cell cultures

(A) Schematic representation of the experimental design. Primary mouse CP cell cultures, taken from WT mice, were exposed to 24-OH or DMSO control for either 12 h or 24 h.

(B) Expressional response of the cholesterol homeostasis signature genes *Abcg1*, *Abca1*, and *Hmgcr* in primary mouse CP cell cultures to increasing concentrations of 24-OH relative to DMSO control (24-OH, 0 μM), after 24 h incubation, measured by qRT-PCR. Sample numbers of wells: *Abcg1* and *Abca1*, 24-OH (0 μM), n = 3; 24-OH (0.1 μM), n = 4; 24-OH (1 μM), n = 4; 24-OH (10 μM), n = 3; *Hmgcr*, 24-OH (0 μM), n = 3; 24-OH (0.1 μM), n = 3; 24-OH (1 μM), n = 4; 24-OH (10 μM), n = 3. Statistical analysis: For each gene, one-way ANOVA followed by Tukey's post hoc test.

(C–F) Bulk RNA-seq of primary mouse CP cell cultures exposed to 24-OH or DMSO control for 12 h or 24 h, combined. Merged results from three experiments. Sample numbers of wells: DMSO, n = 7; 24-OH, n = 12. See also Figure S3 and Table S2. (C) Bar plot of differentially expressed cholesterol homeostasis genes (FDR-adjusted Wald's test $p < 0.050$). (D) Pathway enrichment analysis of highly differentially upregulated genes ($log_2fc > 1.000$, FDR-adjusted Wald's test $p < 0.050$). (E) Pathway enrichment analysis of highly differentially downregulated genes ($log_2fc < -1.000$, FDR-adjusted Wald's test $p < 0.050$). (D and E) Graphs show the top non-redundant enrichment clusters. (F) Volcano plot showing the effect of 24-OH on selected genes related to key inflammatory pathways (IFN-I, interleukins, complement, CCL/CXCL chemokines) in primary mouse CP cell cultures. Yellow: $log_2fc < -1.000$, FDR-adjusted Wald's test $p < 0.050$; dark red: $log_2fc > 1.000$, FDR-adjusted Wald's test $p < 0.050$.

In (B) and (C), bars represent the mean ± standard error of the mean.

enriched in epithelial cells,[35] the major cell type expressing CYP46A1 (Figure 1). Based on previous findings in the TR-CSFB3 CP cell line,[21] we exposed primary mouse CP cell cultures to different concentrations of 24-OH (0.1–10 μM) using DMSO as control (Figure 3A). Consistent with the aforementioned study,[21] we observed a concentration-dependent upregulation of the LXR-dependent genes *Abca1* and *Abcg1* (Figure 3B). In addition, we found a concentration-dependent downregulation of the *Hmgcr* gene, encoding the rate-controlling enzyme of cholesterol synthesis (Figure 3B). Considering these results, we selected the concentration of 24-OH that yielded the maximum response (10 μM; Figure 3B), and performed bulk RNA sequencing (RNA-seq) on primary mouse CP cell cultures to identify the global transcriptional programs regulated by 24-OH in the mouse CP. By pooling the gene expression profiles following 12- and 24-h exposure to 24-OH, which were similar (Figure S3), we observed significant differential expression for 3,515 genes (DESeq2, FDR-adjusted Wald's test $p < 0.050$). A majority of 2,009 differentially expressed genes showed downregulation, while the remaining 1,506 genes were found to be upregulated in response to 24-OH stimulation (Table S2). As expected,[36] 24-OH increased the expression of genes associated with reverse cholesterol transport, such as *Abca1*, *Abcg1*, and *Apoe*, and repressed genes required for cholesterol synthesis, including *Hmgcr*, *Hmgcs1*, and *Sqle* as well as genes involved in cholesterol import, such as *Ldlr* (Figure 3C). Pathway enrichment analysis of the highly differentially expressed genes ($log_2fc > |1.000|$, FDR-adjusted Wald's test $p < 0.050$) revealed that the top upregulated pathways were related to various aspects of cellular dynamics and regulation, such as nuclear chromosome segregation and actinfilament-based process (Figure 3D). Conversely, the top downregulated pathways were prominently associated with immune and inflammatory responses (Figure 3E). The downregulated pathways exhibited overall higher gene counts compared with the upregulated pathways, suggesting a broader impact on the associated biological processes (Figures 3D and 3E). Among the downregulated inflammatory genes, we found transcripts that encode type

I interferon (IFN-I) signaling molecules, interleukins, complements, and CCL/CXCL chemokines (Figure 3F), previously linked to impaired cognitive function in aging, neurodegeneration, and viral infection.[3–6,8,9,30,37–39]

24-OH downregulates disease-associated CP inflammatory signatures conserved across multiple conditions

Drawing from the above findings (Figures 2 and 3) and given that CP inflammation is a common hallmark in multiple brain conditions in humans and mouse models,[3,4,6,30,40–42] we hypothesized that the inflammatory genes downregulated by 24-OH in the CP cell cultures might represent genes that are commonly upregulated in the CP across diverse neurological conditions. To this end, we reanalyzed publicly available CP transcriptome datasets related to several brain conditions. The conditions considered included mouse aging (21 months relative to 3 months[25]) and chronic human neurodegenerative diseases such as AD,[30] frontotemporal dementia (FTD),[30] Huntington's disease (HD),[30] and progressive multiple sclerosis (PMS).[40] We also included human COVID[3] in our study, for the same rationale put forth above. Each dataset was separately analyzed, and genes were selected based on cutoffs for differential expression and statistical significance specific for each condition ($\log_2$fc > |0.500| and FDR-adjusted $p < 0.050$ for mouse aging, AD, and COVID; $\log_2$fc > |0.500| and non-adjusted $p < 0.050$ for FTD, HD, and PMS; Table S3). We compared the list of the differentially expressed genes in each brain condition with the list of the highly differentially expressed genes in primary mouse CP cell cultures exposed to 24-OH ($\log_2$fc > |1.000| and FDR-adjusted Wald's test $p < 0.050$). Overall a consistent pattern emerged, revealing that the majority of the genes shared between the 24-OH dataset and each brain condition dataset were downregulated in the 24-OH dataset and upregulated in each brain condition dataset (Figure 4A).

Among the brain conditions considered above, aging, AD, and COVID are characterized by decreased levels of CYP46A1 expression in the CP (Figure 2) and increased inflammatory transcriptomic signatures.[3–6,30–32] Hence, we hypothesized that the 24-OH effect on the CP may provide a functional link in these conditions. We focused on the shared genes between those downregulated in the 24-OH dataset and those upregulated in the mouse aging, human AD, and human COVID datasets (Figure 4B). We found that the serine protease inhibitor gene *SERPINA3*, an AD risk factor[43] that was shown to be upregulated in other diseases characterized by cognitive impairment such as prion diseases[44] as well as in schizophrenia,[41] was found here to be shared across the mouse aging, human AD, and human COVID datasets (Figure 4B). In addition, the complement cascade genes *C1S* and *C3*, and the IFN-I-related gene *IFITM3*, were commonly upregulated in the mouse aging and COVID datasets (Figure 4B). To gain a comprehensive understanding of the biological processes that were upregulated across the mouse aging, AD, and COVID datasets, and downregulated in the 24-OH dataset, we performed pathway enrichment analysis and found a strong association with cytokine signaling and innate immune response pathways (Figure 4C). Additionally, to explore the relationships between the identified differentially expressed genes, we conducted protein-protein interaction analysis. Notably, we found IFN-I signaling to be the most significant protein-protein interaction complex (Figure 4D). Chronic elevation of IFN-I signaling in the CP has been shown to cause cognitive impairment by directly triggering a hyperactive microglial state.[5] Overall, our *in silico* analyses revealed that 24-OH suppressed CP inflammatory signatures that were found here to be commonly expressed across multiple brain disease states in mice and humans that have been previously linked to cognitive impairment.

Inverse relationships between CYP46A1 and TNF-α inflammation in the CP

Our results (Figures 3 and 4) suggested that boosting 24-OH signaling in the CP could increase its resilience to inflammatory signals. Analysis of the transcriptional regulatory networks of the genes that exhibited considerable downregulation in response to 24-OH in primary mouse CP cell cultures ($\log_2$fc < −1.000, FDR-adjusted Wald's test $p < 0.050$) revealed nuclear factor (NF)-κB1 and RELA as the top predicted transcription factors (Figure 5A). Similarly, RELA and NF-κB1 were the top predicted regulators of the genes that were downregulated in the 24-OH dataset and also upregulated across the mouse aging, AD, and COVID datasets (Figures 4B and 5B). NF-κB1 and RELA are both involved in the activation of the NF-κB inflammatory pathway, which is notably repressed by LXRs.[11] One of the best known inducers of the NF-κB pathway is the pro-inflammatory cytokine TNF-α.[45] Building on these insights, we delved deeper into the understanding of the interplay between CYP46A1/24-OH and TNF-α in the CP. To this end, we first studied the effect of TNF-α on *Cyp46a1* gene expression in primary mouse CP cell cultures, using the same conditions as in our previous studies.[4,35,46] We found a significant decrease in *Cyp46a1* expression upon exposure to TNF-α (Figure 5C), which was neutralized with the antibody directed to the TNF-α receptor TNFR1 but not to TNFR2 (Figure 5D). Examining the mouse CP atlas[22] revealed that both *Tnfrsf1a* and *Tnfrsf1b* genes, encoding TNFR1 and TNFR2, respectively, are expressed in CP epithelial cells and that *Tnfrsf1a* shows predominant expression (Figure S4A). Similar expression patterns for the homologous *TNFRSF1A* and *TNFRSF1B* genes were found in the spatial map of the human CP[3] (Figure S4B). Taken together, these findings revealed that TNFR1 mediates the effect of TNF-α on mouse CYP46A1 and that this mechanism may be conserved in humans.

We next established *ex vivo* mouse CP organ cultures to more closely simulate the response of the CP *in vivo* as a complex tissue, in order to investigate whether and how enhancing CYP46A1 expression or enzymatic activity in the CP might affect its response to TNF-α. In establishing this experimental condition, we evaluated the response of mouse CP organ cultures to the same stimuli used throughout the study on primary mouse CP cell cultures: 24-OH (Figure 3) and TNF-α (Figures 5C and 5D). Specifically, we confirmed that 24-OH regulated signature genes related to cholesterol homeostasis in a concentration-dependent manner (Figures S5A and S5B) and that TNF-α downregulated *Cyp46a1* gene expression (Figures S5C and S5D), consistent with the effects observed in primary mouse CP cell

CellPress
OPEN ACCESS

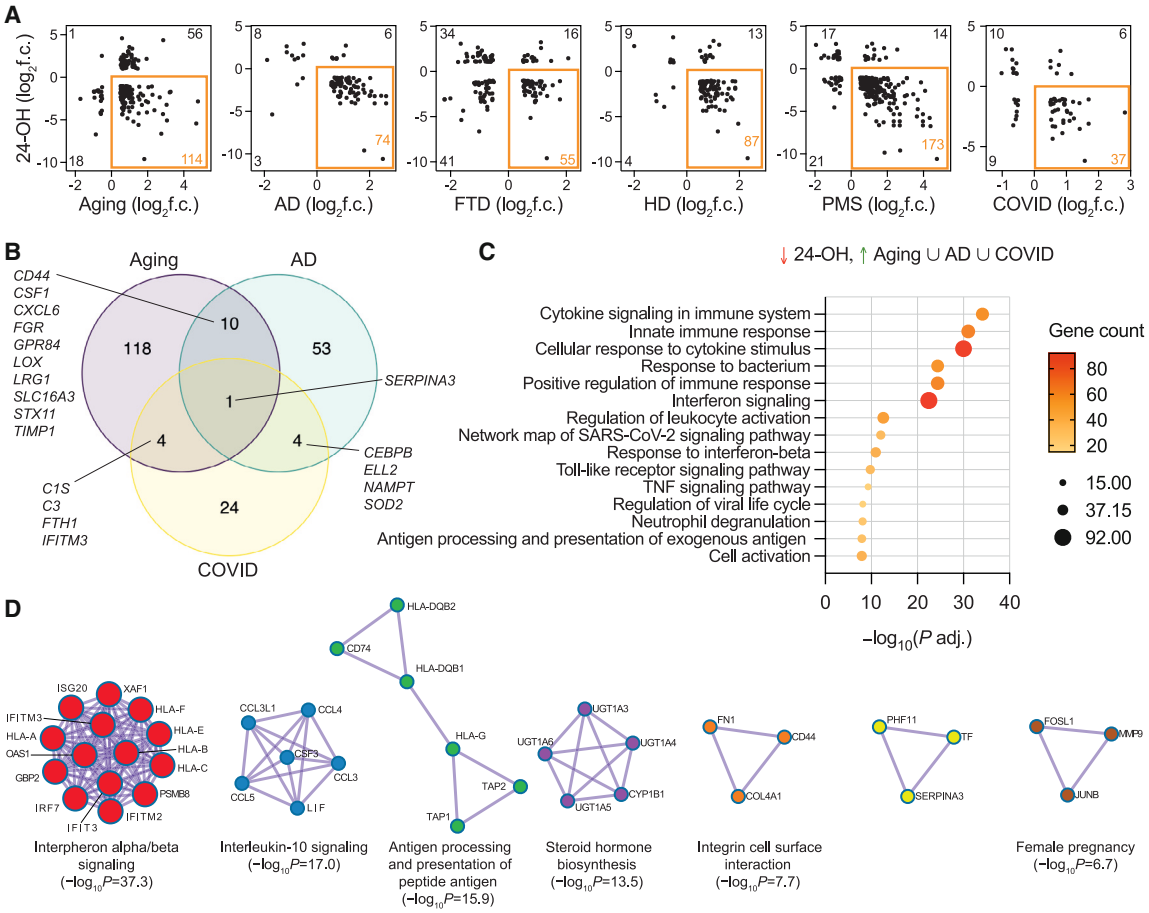

Figure 4. 24-OH suppressed inflammatory signatures *in vitro* that are commonly elevated in the CP across multiple brain conditions

(A) Relationships between differential expression profiles in primary mouse CP cell cultures treated with 24-OH ($log_2fc > |1.000|$, FDR-adjusted Wald's test $p < 0.050$) and differentially expressed genes in the CP in different brain conditions in mouse and humans: mouse aging (21 months relative to 3 months; $log_2fc > |0.500|$, FDR-adjusted $p < 0.050$), human AD ($log_2fc > |0.500|$, FDR-adjusted $p < 0.050$), human FTD ($log_2fc > |0.500|$, non-adjusted $p < 0.050$), human HD ($log_2fc > |0.500|$, non-adjusted $p < 0.050$), human PMS ($log_2fc > |0.500|$, non-adjusted $p < 0.050$), and human COVID ($log_2fc > |0.500|$, FDR-adjusted $p < 0.050$). See also Table S3. The orange boxes encase the genes that were found to be downregulated in the 24-OH dataset and upregulated in each brain condition dataset. Gene counts are shown in each quadrant. The 24-OH dataset is the one described in Figures 3C–3F. The mouse aging dataset was the same as utilized for the analyses described in Figures 2L and S2A–S2N. The AD, FTD, and HD datasets were retrieved from Stopa et al.[30] The PMS dataset was retrieved from Rodríguez-Lorenzo et al.[40] The COVID dataset was the same as utilized for the analyses described in Figure 2M, calculating for each gene the average expression across all cell types.

(B) Venn diagram of the differentially expressed genes that were downregulated in the 24-OH dataset (human orthologs; $log_2fc < -1.000$, FDR-adjusted Wald's test $p < 0.050$) and upregulated in the mouse aging (human orthologs), human AD, and/or human COVID datasets ($log_2fc > 0.500$, FDR-adjusted $p < 0.050$).

(C) Pathway enrichment analysis of the union of the three differentially expressed gene sets described in (B). The graph shows the top non-redundant enrichment clusters.

(D) Protein-protein interaction analysis of the union of the three differentially expressed gene sets described in (B). Automatically identified networks are colored based on their identities and annotated based on the top functional enriched term, if available.

cultures (Figures 3A, 3B, 5C, and 5D). As a next step, we chose, as experimental readouts, TNF-α-inducible genetic signatures, based on existing literature, that were found here to be downregulated by 24-OH in primary mouse CP cell cultures ($log_2fc < -1.000$, FDR-adjusted Wald's test $p < 0.050$) and upregulated in the CP across neuropathological states ($log_2fc > 0.500$, non-adjusted $p < 0.050$; Figure S5E). Experimental validation by qRT-PCR confirmed upregulation of *C3*, *C1ra*, *Sod2*, and *Tlr2* in primary mouse CP organ cultures exposed to TNF-α (Figure S5F). Subsequently, we infected mouse CP organ cultures with an adeno-associated virus serotype 1 (AAV1) viral construct expressing mouse CYP46A1 (AAV_mCYP46A1) or green fluorescent protein (AAV_GFP) as control. We observed a robust and significant elevation of *Cyp46a1* transcript levels in AAV_mCYP46A1-infected cultures compared with AAV_GFP-infected as well as non-infected control cultures (Figure 5E). Using IHC, we confirmed CYP46A1 protein overexpression in cultures infected with AAV_mCYP46A1 relative to AAV_GFP-infected controls (Figures 5F and 5G). Using these conditions, we infected mouse CP organ cultures with AAV_mCYP46A1 or

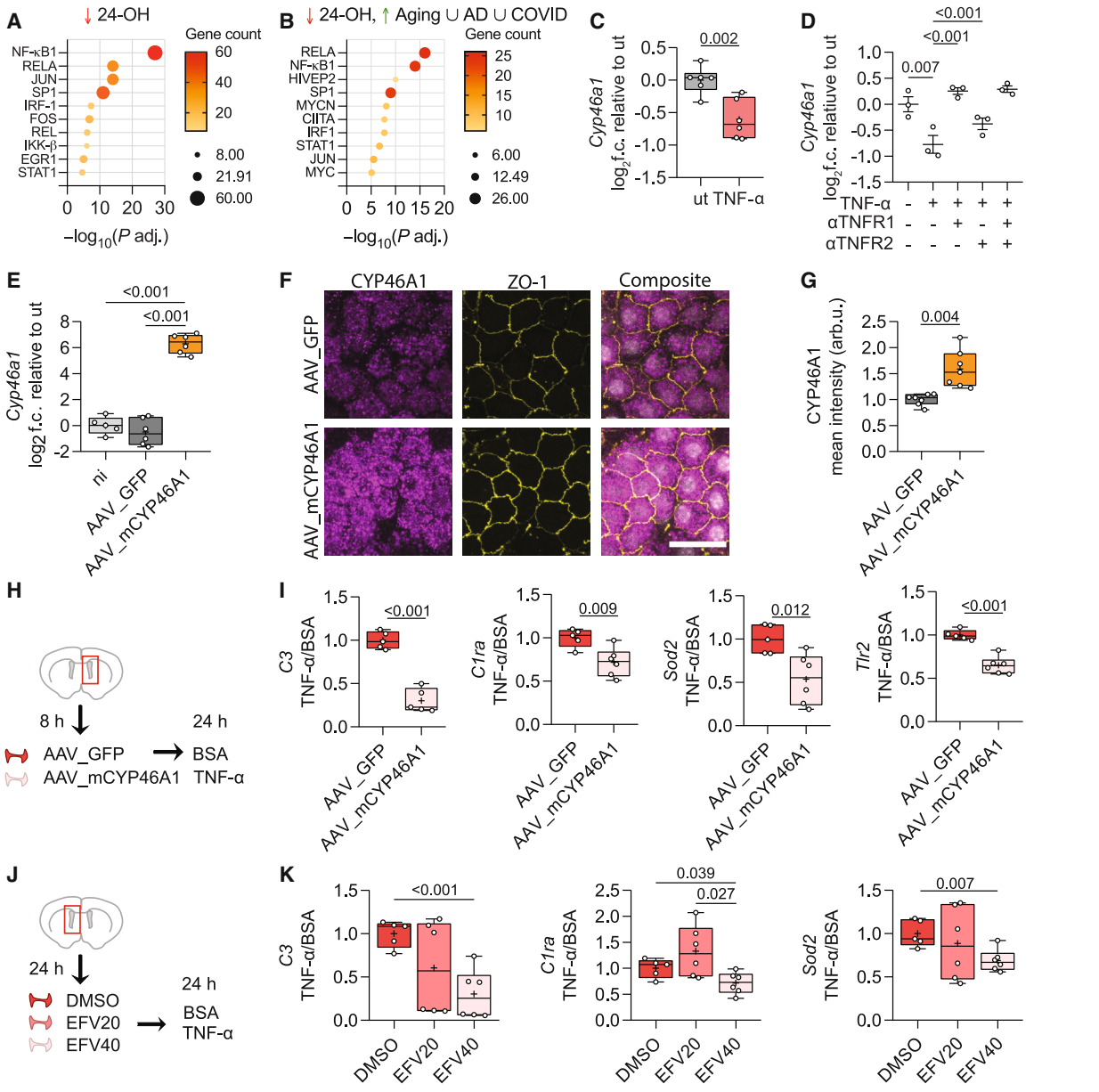

Figure 5. Enhancing CYP46A1 expression or enzymatic activity in mouse CP organ cultures attenuated TNF-α-dependent inflammatory responses

(A) Transcriptional regulatory network analysis of the genes that were highly differentially downregulated by 24-OH in primary mouse CP cell cultures ($log_2fc < -1.000$, FDR-adjusted Wald's test $p < 0.050$).

(B) Transcriptional regulatory network analysis of the genes that were downregulated in the 24-OH dataset (human orthologs; $log_2fc < -1.000$, FDR-adjusted Wald's test $p < 0.050$) and upregulated in the mouse aging (human orthologs), human AD, and/or human COVID datasets ($log_2fc > 0.500$, FDR-adjusted $p < 0.050$).

(C) *Cyp46a1* gene expression in primary mouse CP cell cultures following 24-h stimulation with 100 ng/mL TNF-α relative to medium-only control (untreated, ut), measured by qRT-PCR. Merged results from two experiments. Sample numbers of wells: ut, n = 6; TNF-α, n = 6. Statistical analysis: two-tailed unpaired Student's t test.

(D) *Cyp46a1* gene expression in primary mouse CP cell cultures following 24-h stimulation with 100 ng/mL TNF-α relative to medium-only control (untreated, ut), with or without TNFR1 or TNFR2 neutralizing antibodies (αTNFR1 and αTNFR2, respectively), measured by qRT-PCR. Sample numbers of wells: ut, n = 3; TNF-α, n = 3; TNF-α + αTNFR1, n = 3; TNF-α + αTNFR2, n = 3; TNF-α + αTNFR1 + αTNFR2, n = 3. Statistical analysis: one-way ANOVA followed by Tukey's post hoc test. See also Figure S4.

(E–G) Overexpression of *Cyp46a1* gene in mouse CP organ cultures. CP tissue from the left lateral ventricle was incubated for 8 h with AAV_mCYP46A1 or AAV_GFP control viruses. See also Figure S5. (E) *Cyp46a1* gene expression in mouse CP organ cultures infected with AAV_mCYP46A1 or AAV_GFP relative to non-infected (ni) controls, measured by qRT-PCR. Merged results from two experiments. Sample numbers of mice: ni, n = 5; AAV_GFP, n = 6; AAV_mCYP46A1,

(legend continued on next page)

AAV_GFP control and subsequently exposed the same cultures to TNF-α or bovine serum albumin (BSA) control (Figure 5H). We found that CYP46A1 overexpression *ex vivo* attenuated the expression of the tested TNF-α responsive genes *C3*, *C1ra*, *Sod2*, and *Tlr2* relative to AAV_GFP control cultures (TNF-α versus BSA response fold change, normalized by the AAV_GFP group; Figure 5I). Additionally, we employed an alternative approach of pharmacologically enhancing CYP46A1 enzymatic activity by exposing mouse CP organ cultures to efavirenz, a CYP46A1 agonist drug,[47] using DMSO control, and subsequently to TNF-α or BSA control (Figure 5J). Consistent with *Cyp46a1* overexpression (Figures 5H and 5I), enhancing CYP46A1 activity with increasing efavirenz concentration[48] attenuated the TNF-α responsive genes *C3*, *C1ra*, and *Sod2* (TNF-α versus BSA response fold change, normalized by the DMSO group; Figure 5K). These results indicate that increasing CP CYP46A1 expression or enzymatic activity enhanced resilience to TNF-α-dependent inflammatory responses.

CYP46A1 overexpression in the CP in 5xFAD mice attenuated brain inflammation

To investigate the potential impact of CYP46A1 overexpression specifically in the CP on the brain *in vivo*, we injected bilaterally intracerebroventricularly AAV_mCYP46A1 virus or AAV_GFP control to 5xFAD mice (Figure 6A). The injections were carried out at 8–11 months to allow behavioral testing at 9–12 months (Figure 6A). For behavioral assessment we used the novel object recognition assay (NOR; Figure 6A), which effectively captures decline of recognition memory, starting in this mouse model at this disease stage.[49,50] Non-injected, age-matched WT mice were included to set the baseline for normal NOR behavior. AAV_mCYP46A1 5xFAD mice exhibited significantly higher recognition memory scores than AAV_GFP 5xFAD mice and performed at a level akin to that of non-injected WT controls (Figure 6B). After behavioral assessment, the mice were euthanized and their brains collected for further analyses. To rule out CP epithelial cell death associated with AAV infection, we stained for cleaved caspase-3 and found no differences compared with non-injected WT mice as well as between the two AAV groups (Figures S6A and S6B). To evaluate the success of infection, we measured GFP expression in brain sections from AAV_GFP 5xFAD mice (Figure S6C). In addition to the presence of GFP^+ cuboidal cells in the CP, indicating targeting of the epithelial cell layer, we found evidence of some viral leakage in the hippocampus and cortex (Figure S6C), which we independently confirmed by measuring the expression of the viral gene *wpre* in some of the AAV-injected mice used throughout the study (Figure S6D–S6F). We therefore examined the expression of *Cyp46a1* in the CP, hippocampus, and cortex of the mice that were included in the behavioral tests to verify the efficiency of CP infection and determine the levels of off-target *Cyp46a1* overexpression in the brain parenchyma (Figures S6G–S6I). To minimize off-target *Cyp46a1* overexpression effects, for further analyses we included only the AAV_mCYP46A1 mice with robust *Cyp46a1* overexpression in the CP ($log_2fc > 2.000$; Figure S6G) and relatively moderate overexpression in the hippocampus ($log_2fc < 1.000$; Figure S6H), hereafter referred to as "AAV_mCYP46A1 included" (AAV_mCYP46A1^{in}) mice. Cortical *Cyp46a1* expression measured in some of the AAV_mCYP46A1^{in} mice revealed significant but only marginal overexpression ($log_2fc < 1.000$; Figure S6I). The detailed exclusion process is described in STAR Methods, "exclusion criteria for AAV_mCYP46A1 mice."

Reanalyzing the NOR data of the remaining AAV_mCYP46A1^{in} mice (Figure 6C) revealed consistent results with those prior to the exclusion (Figure 6B). Locomotor activity and anxiety levels were comparable between AAV_mCYP46A1^{in} and AAV_GFP 5xFAD mice (Figures S6J and S6K). Of note, the distribution of the memory recognition scores of the AAV_mCYP46A1 mice that were excluded due to high *Cyp46a1* expression in the hippocampus (4 mice) was comparable to that of the AAV_mCYP46A1^{in} mice (15 mice; *F*-test $p = 0.567$), indicating that off-target overexpression did not contribute to the behavioral outcome beyond the impact of the targeted overexpression in the CP (Figure 6B).

Next, we assessed whether the overexpression of *Cyp46a1* had any impact on the inflammatory fate of the CP. We found

n = 6. Statistical analysis: one-way ANOVA followed by Tukey's post hoc test. (F) Representative images of AAV-infected whole-mount mouse CP organ cultures (maximum-intensity projections). ZO-1 stains for epithelial tight junctions. Composite images show Hoechst-counterstained cell nuclei in white. Scale bar, 20 μm. (G) Quantification of CYP46A1 levels in sum intensity projections of confocal z stacks, calculated as mean gray value of the stained area divided by the stack's depth; arb. u., arbitrary units. Merged results from two experiments. Sample numbers of mice: AAV_GFP, n = 7; AAV_mCYP46A1, n = 7. Statistical analysis: two-tailed unpaired Student's t test with Welch's correction.

(H and I) Overexpression of *Cyp46a1* in mouse CP organ cultures followed by TNF-α challenge. (H) Schematic representation of the experimental design. CP tissue from the left lateral ventricle, one individual mouse per well, was incubated for 8 h with AAV_mCYP46A1 or AAV_GFP control viruses, and subsequently treated for 24 h with 20 ng/mL TNF-α or BSA control. (I) Expressional response of selected genes (see results for details), quantified as TNF-α/BSA fold changes, measured by qRT-PCR. The TNF-α/BSA fold changes represent the values of TNF-α-treated samples divided by their corresponding BSA-treated samples (n = 3 for each experiment) in both the AAV_GFP and AAV_mCYP46A1 groups. These fold changes were normalized by the AAV_GFP control group. Merged results from two experiments. Sample numbers of mice: *C1ra*, *Sod2*, *Tlr2*, AAV_GFP, n = 5; AAV_mCYP46A1, n = 6; *C3*, AAV_GFP, n = 5; AAV_mCYP46A1, n = 5. Statistical analysis: two-tailed unpaired Student's t test.

(J and K) Pharmacological activation of CYP46A1 enzyme in mouse CP organ cultures followed by TNF-α challenge. (J) Schematic representation of the experimental strategy. CP tissue from the right lateral ventricle, one individual mouse per well, was incubated for 24 h with increasing concentrations of the CYP46A1 agonist drug efavirenz (20 μM, EFV20; 40 μM, EFV40) or DMSO control, and subsequently treated for 24 h with 20 ng/mL TNF-α or BSA (control). (K) Expressional response of selected genes (see results for details), quantified as TNF-α/BSA fold changes, measured by qRT-PCR. The TNF-α/BSA fold changes represent the values of TNF-α-treated samples divided by their corresponding BSA-treated samples (n = 3 for each experiment) in the DMSO, EFV20, and EFV40 groups. These fold changes were normalized by the DMSO control group. Merged results from two experiments. Sample numbers of mice: DMSO, n = 5; EFV20, n = 6; EFV40, n = 6. Statistical analysis: Brown-Forsythe and Welch's ANOVA tests followed by unpaired Student's t test with Welch's correction.

In (C)–(E), (G), (I), and (K), the box plots present the minimum and maximum values (whiskers), the first and third quartiles (box boundaries), the median (box internal line), and the mean (cross).

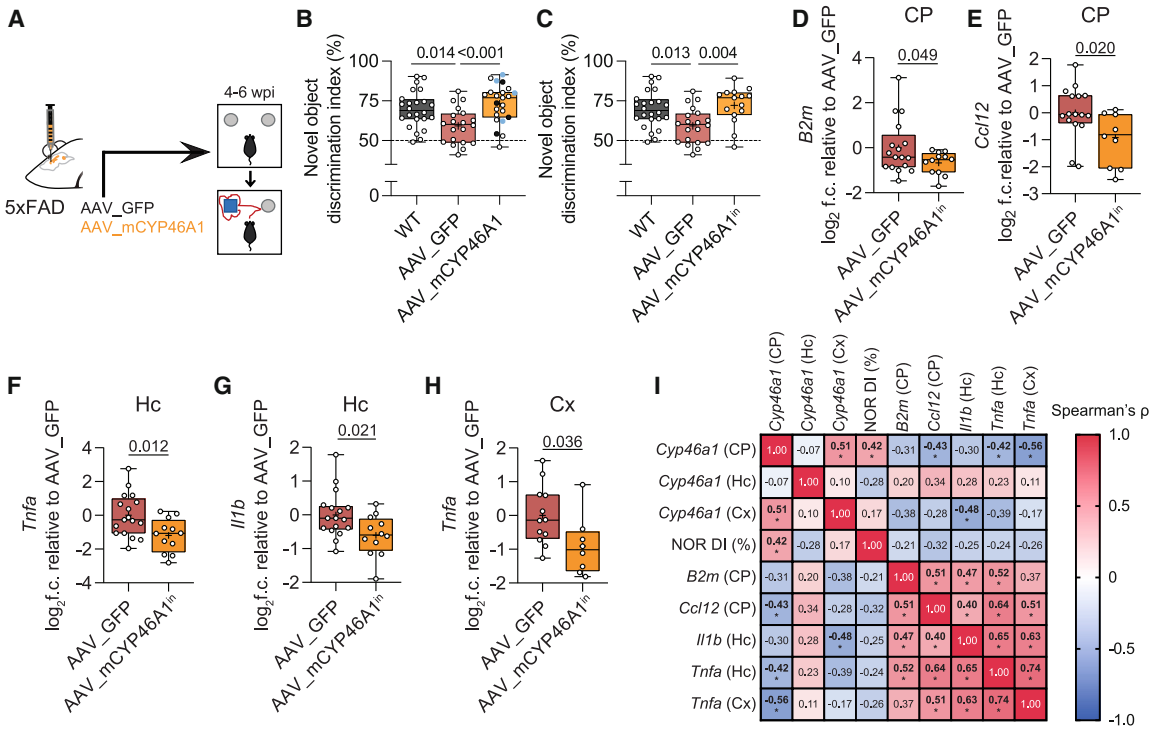

Figure 6. *Cyp46a1* gene overexpression in the CP was associated with improved recognition memory and attenuated brain inflammation in 5xFAD mice

(A–C) Evaluation of the impact of *Cyp46a1* gene overexpression in the CP on memory recognition in 5xFAD mice. (A) Schematic representation of the experimental design. 5xFAD mice received bilateral intracerebroventricular injections of AAV_mCYP46A1 or AAV_GFP control viruses and their recognition memory ability was tested using the NOR task at 4–6 weeks post injection (wpi). See also Figures S6A–S6I. (B and C) Analysis of recognition memory performance in the NOR task. y-axis break was used to enhance readability of the dynamic range of the data. (B) Analysis of recognition memory ability including all AAV_mCYP46A1 mice. Light-blue dots represent mice with relatively low *Cyp46a1* expression in the CP (log_2fc < 2.000), whereas black dots represent mice with relatively high *Cyp46a1* expression in the hippocampus (log_2fc > 1.000), as identified following the analyses described in Figures S6G–S6I. Merged results from four experiments. Sample numbers of mice: WT, n = 24; AAV_GFP, n = 20; AAV_mCYP46A1, n = 23. (C) Analysis of recognition memory ability including only the AAV_mCYP46A1 mice with high *Cyp46a1* expression in the CP (log_2fc > 2.000) and low off-target *Cyp46a1* expression in the hippocampus (log_2fc < 1.000; AAV_mCYP46A1^{in}). (B and C) Merged results from four experiments. Sample numbers of mice: WT, n = 24; AAV_GFP, n = 20; AAV_mCYP46A1, n = 15. Statistical analysis: one-way ANOVA followed by Tukey's post hoc test. See also Figures S6J and S6K.

(D and E) Expression of the inflammatory marker genes *B2m* (D) and *Ccl12* (E) in the CP in AAV_mCYP46A1^{in} and AAV_GFP mice, measured by qRT-PCR. Merged results from three experiments. Sample numbers of mice: (D) AAV_GFP, n = 17; AAV_mCYP46A1^{in}, n = 12; (E) AAV_GFP, n = 16; AAV_mCYP46A1^{in}, n = 11. Statistical analysis: (D) two-tailed unpaired Student's t test with Welch's correction; (E) two-tailed unpaired Student's t test.

(F–H) Expression of the inflammatory marker genes *Tnfa* and *Il1b* in the hippocampus (Hc; F and G, respectively) and *Tnfa* in the cortex (Cx; H) in AAV_mCYP46A1^{in} and AAV_GFP mice, measured by qRT-PCR. See also Figures S6L–S6Q. (F and G) Merged results from three experiments. Sample numbers of mice: AAV_GFP, n = 17; AAV_mCYP46A1, n = 12. (H) Merged results from two experiments. Sample numbers of mice: AAV_GFP, n = 12; AAV_mCYP46A1, n = 8. (F–H) Statistical analysis: two-tailed unpaired Student's t test.

(I) Correlation matrix showing the pairwise Spearman's rank correlations between NOR discrimination index (DI) and expression levels of *Cyp46a1* and other inflammatory marker genes in the CP, hippocampus, and cortex across AAV_GFP and AAV_mCYP46A1^{in} mice. The color code indicates magnitude and direction of the correlation, with red shades representing positive correlations, white representing no correlation, and blue shades representing negative correlations. Spearman's rank correlation ρ coefficients are shown inside the matrix. Asterisks denote statistically significant correlations (two-tailed p < 0.050). For *Cyp46a1* (CP), *Cyp46a1* (Hc), *Cyp46a1* (Cx), and NOR DI (%), merged results from four experiments. Sample numbers of mice: *Cyp46a1* (CP), *Cyp46a1* (Hc) and NOR DI (%), AAV_GFP, n = 20; AAV_mCYP46A1, n = 15; *Cyp46a1* (Cx), AAV_GFP, n = 15; AAV_mCYP46A1, n = 11. For *B2m* (CP), *Il1b* (Hc), *Tnfa* (Hc), and *Ccl12* (CP), merged results from three experiments. Sample numbers of mice: *B2m* (CP), *Il1b* (Hc), and *Tnfa* (Hc), AAV_GFP, n = 17; AAV_mCYP46A1, n = 12; *Ccl12* (CP), AAV_GFP, n = 16; AAV_mCYP46A1, n = 11. For *Tnfa* (Cx), merged results from two experiments. Sample numbers of mice: AAV_GFP, n = 12; AAV_mCYP46A1, n = 8.

In (B)–(H), the box plots present the minimum and maximum values (whiskers), the first and third quartiles (box boundaries), the median (box internal line), and the mean (cross).

that *B2m*, previously linked to cognitive loss[51] and IFN-I signaling in the CP,[5] was decreased in AAV_mCYP46A1^{in} 5xFAD mice compared with AAV_GFP 5xFAD mice (Figure 6D). We also found a decrease in the CP of the IFN-I-inducible chemokine[52] *Ccl12* (Figure 6E). Examination of AD-related pathological hallmarks in the 5xFAD model,[49,53,54] such as water-soluble and insoluble amyloid-β1–42 amounts in the hippocampus and gliosis, revealed no differences between the two AAV groups (Figures S6L–S6Q). Notably, however, AAV_mCYP46A1^{in} 5xFAD mice showed decreased expression of *Tnfa* and *Il1b* in

the hippocampus (Figures 6F and 6G) as well as decreased expression of *Tnfa* in the cortex (Figure 6H). Further analyses revealed a significant positive correlation between *Cyp46a1* expression in the CP and cognitive performance in the NOR assay (Figure 6I) and a significant negative correlation with markers of inflammation (*Ccl12* in the CP and *Tnfa* in the hippocampus and cortex; Figure 6I). In contrast, *Cyp46a1* expression in the cortex was significantly negatively correlated with *Il1b* expression in the hippocampus, but no significant association emerged with the other outcomes, particularly recognition memory (Figure 6I). No correlation was found between *Cyp46a1* expression in the hippocampus and any of the outcomes. Overall, our results suggest that targeted CYP46A1 overexpression in the CP could be beneficial to the cognitive outcome in AAV_mCYP46A1^{in} 5xFAD mice via the overall amelioration of the CP inflammatory milieu.

Based on our previous work demonstrating that the inflammatory milieu of the CP affects the fate of the microglia,[5] we considered that the reduced brain inflammation in the AAV_mCYP46A1 mice could be manifested in the microglial profile. We therefore sorted CD45^{+}CD11b^{+} myeloid cells, which include mainly microglia and some infiltrating monocyte-derived macrophages,[53] from AAV_mCYP46A1^{in} and AAV_GFP mice and found reduced expression of the IFN-I-related genes *C4b* and *B2m* in AAV_mCYP46A1^{in} mice (Figures S6R and S6S). This observation is intriguing in light of the previous findings of increased microglial expression of *C4b* and *B2m* in aged mice as well as in middle-aged mice overexpressing IFN-I in the CP.[5] This finding further supports our contention that the benefit of *Cyp46a1* overexpression in AAV_mCYP46A1^{in} 5xFAD mice is linked to the effects of increased CYP46A1 activity within the CP on the immune milieu of the CP itself, which in turn could potentially affect the immune fate of microglia.[5]

DISCUSSION

In the present study, we demonstrated that the brain-specific enzyme CYP46A1 is expressed in the CP epithelium of mouse and human brains, and we showed that its expression is decreased under different neurological conditions. *In vitro* experiments with mouse primary CP cells and organ cultures revealed that, while CYP46A1 levels decreased in response to TNF-α, boosting CYP46A1 expression or enzymatic activity increased the resilience of the CP to this cytokine. Moreover, *in vivo* experiments with 5xFAD mice indicated that overexpression of CYP46A1 in the CP had a beneficial effect on cognitive performance via reduced CP inflammation and consequential brain inflammation. In line with this, the enzymatic product of CYP46A1, 24-OH, broadly suppressed immune and inflammatory pathways in the CP, suggesting an anti-inflammatory effect of CYP46A1 on the CP via 24-OH.

Previous research has primarily investigated neuronal CYP46A1 and its function in regulating cholesterol levels in the healthy and diseased brain.[18] In line with this, 24-OH was shown to stimulate cholesterol export at the CP.[21] Our finding that the inflammatory state of the CP is affected both by CP CYP46A1 activation and by stimulation with 24-OH suggests a physiological role for CP-derived 24-OH in the regulation of CP immune homeostasis, which is, in turn, central to brain function. In aging and chronic neurodegeneration, but also in viral infections and schizophrenia, inflammation of the CP is associated with the increased production of cytokines and other signaling molecules, leading to the dysregulation of CP genes involved in the modulation of barrier properties, CSF composition, neurotrophic support, and microglial activity.[4,6,30–33,39–42] In particular, cumulative evidence points out increased expression of IFN-I signaling in the CP as a common occurrence in multiple brain conditions,[3,4,6,30] in line with our results here from reanalyzing previously published datasets. IFN-I signaling at the CP can directly cause brain inflammation and cognitive dysfunction by deregulation of microglial homeostasis.[5,55] Therefore, controlled levels of CYP46A1 in the CP may help restrain the propagation of inflammation within the brain parenchyma and protect cognitive function. Nonetheless, we cannot rule out the possibility that CYP27A1, which we found here to be more abundantly expressed than CYP46A1 in the human CP, has an impact as well via its product, 27-hydroxycholesterol.

Previous studies reported decreased levels of CYP46A1 in various brain regions in different neurodegenerative diseases, such as tauopathy,[56] HD,[57] Machado-Joseph disease,[58] and prion disease.[59] Consistently, we found mild but significant decrease in CYP46A1 expression in the CP at the RNA and/or protein level under conditions of brain amyloidosis (5xFAD mice), during aging (mice and human postmortem samples), and in individuals who died of COVID. We also found that changes in CYP46A1 levels in the CP did not correspond to alterations in the brain parenchyma in the same conditions. The decreased expression of CYP46A1 in the CP in 5xFAD mice, in individuals with advanced age, and in COVID victims did not appear to depend on the loss of CP epithelial cells under the tested conditions. Instead, CP CYP46A1 reduction in these conditions could be explained by the accumulation of TNF-α within the CSF,[60,61] supported by our findings showing a negative effect of TNF-α on CP CYP46A1 expression. Conversely, we provide evidence that enhancing CYP46A1 expression or enzymatic activity *in vitro* rendered the CP more refractory to the action of TNF-α. In line with this, in 5xFAD mice overexpressing CYP46A1 in the CP, we observed better cognitive performance in the NOR assay than in AAV_GFP-injected control 5xFAD mice, as well as decreased expression of inflammatory markers in both the CP and the brain. The observed beneficial effects, particularly the cognitive effect, were correlated with the levels of *Cyp46a1* gene expression in the CP and not in the off-target infected areas. Also notably, these beneficial effects were not dependent on the modification of key pathological features of AD, which is in line with the observation in AD patients that the major factor contributing to cognitive loss is local brain inflammation.[62] In particular, the absence of changes in hippocampal amyloid-β42 levels aligns with previous evidence demonstrating that cognitive improvement in 5xFAD mice that were orally administered efavirenz to boost CYP46A1 activity in the brain does not depend on amyloid-β decrease.[63,64]

Overall, our findings are in line with previous studies showing that increasing CYP46A1 expression or enzymatic activity within the brain, or infusing 24-OH into the brain ventricles, have proven

beneficial in a wide range of brain disorders in mouse models.[65,66] Notably, CYP46A1 enzymatic activity mobilizes cholesterol pools and thus may exert local effects in the CP that extend beyond the direct actions of 24-OH, such as regulation of availability of isoprenoid intermediates or signal transduction.[66,67] While further studies are needed to fully understand the mechanisms by which CYP46A1 affects CP biology, our results imply that boosting CYP46A1 expression or enzymatic activity specifically in the CP may benefit the brain by restraining the inflammatory fate of the CP during disease progression, thereby curbing the perpetuation of brain inflammation and preserving brain function. In addition, the inverse relationships between 24-OH and inflammatory signatures in the CP, observed across multiple neurological conditions, suggests that boosting CYP46A1 expression or activity specifically in this compartment has a beneficial effect regardless of disease etiology.

Limitations of the study

Despite our precautions to minimize the confounding effect of viral leakage into the hippocampus and cortex, our *in vivo* overexpression studies have several limitations. First, AAV serotypes with more selective tropism for the CP (e.g., AAV2/5[68,69]) and/or a CP-specific promoter may be a better alternative than AAV1 used here. Second, we cannot rule out the possibility of differences in toxicity between the viral vectors used for the delivery of mCYP46A1 and the control GFP.[70,71]

STAR★METHODS

Detailed methods are provided in the online version of this paper and include the following:

SUPPLEMENTAL INFORMATION

Supplemental information can be found online at https://doi.org/10.1016/j.xcrm.2023.101278.

ACKNOWLEDGMENTS

We thank Alexander Brandis and Tevie Mehlman from the Targeted Metabolomics Unit (Weizmann Institute), Ron Rotkopf from the Bioinformatics unit (Weizmann Institute), and David Gdalevich and Gennady Margolin (Weizmann Institute) for technical support; Shelley Schwarzbaum (Weizmann Institute) for proofreading the manuscript; and Tali Wiesel (Weizmann Institute) for help with the graphical abstract. The work was supported by: the Advanced European Research Council grants 232835 and 741744, the European Seventh Framework Program HEALTH-2011 (279017), the Israel Science Foundation (ISF)-research grant no. 991/16, the ISF-Legacy Heritage Bio-medical Science Partnership research grant no. 1354/15, the Thompson Foundation, and Adelis Foundation (given to M.S.).

AUTHOR CONTRIBUTIONS

A.T.-K., S.S., and M.S. designed, performed, and interpreted the experiments, and wrote the manuscript. A.T.-K. and S.S. performed AAV injections. A.T.-K., S.S., A.S., S.P.C., and M.P. harvested and processed tissues. S.S., A.T.-K., S.P.C., and M.P. performed IHC, imaging, and quantification. A.T.-K. performed behavioral experiments. A.T.-K. performed mouse primary CP cell and organ cultures. A.T.-K., S.S., and A.S. performed qRT-PCR. R.S. performed cloning. R.S., A.T.-K., and M.P. performed western blots. O.S. prepared viruses. M.K. purified RNA, prepared libraries, and performed RNA-seq. E.D. conducted RNA-seq low-level processing. E.F. and A.S. analyzed mouse and human CP transcriptome datasets. S.S. and A.S. performed comparison of mouse and human CP transcriptome datasets. L.C. performed Aβ42 ELISA and genotyping for all mouse lines. O.H. and T.W.-C. provided bulk transcriptome data of mouse brain across lifespan. S.S. and A.T.-K. performed statistical analyses. A.T.-K., S.S., A.S., and M.K. created figures. Y.S. supervised R.S. M.S. and I.A. supervised M.K.

DECLARATION OF INTERESTS

M.S. is an inventor of the intellectual property that forms the basis for the development of PD-L1 immunotherapy for AD.

INCLUSION AND DIVERSITY

We support inclusive, diverse, and equitable conduct of research.

Received: November 15, 2022
Revised: May 26, 2023
Accepted: October 11, 2023
Published: November 8, 2023

REFERENCES

1. Lun, M.P., Monuki, E.S., and Lehtinen, M.K. (2015). Development and functions of the choroid plexus–cerebrospinal fluid system. Nat. Rev. Neurosci. *16*, 445–457.
2. Baruch, K., and Schwartz, M. (2013). CNS-specific T cells shape brain function via the choroid plexus. Brain Behav. Immun. *34*, 11–16.
3. Yang, A.C., Kern, F., Losada, P.M., Agam, M.R., Maat, C.A., Schmartz, G.P., Fehlmann, T., Stein, J.A., Schaum, N., Lee, D.P., et al. (2021). Dysregulation of brain and choroid plexus cell types in severe COVID-19. Nature *595*, 565–571.

4. Baruch, K., Deczkowska, A., David, E., Castellano, J.M., Miller, O., Kertser, A., Berkutzki, T., Barnett-Itzhaki, Z., Bezalel, D., Wyss-Coray, T., et al. (2014). Aging. Aging-induced type I interferon response at the choroid plexus negatively affects brain function. Science *346*, 89–93.

5. Deczkowska, A., Matcovitch-Natan, O., Tsitsou-Kampeli, A., Ben-Hamo, S., Dvir-Szternfeld, R., Spinrad, A., Singer, O., David, E., Winter, D.R., Smith, L.K., et al. (2017). Mef2C restrains microglial inflammatory response and is lost in brain ageing in an IFN-I-dependent manner. Nat. Commun. *8*, 717.

6. Mesquita, S.D., Ferreira, A.C., Gao, F., Coppola, G., Geschwind, D.H., Sousa, J.C., Correia-Neves, M., Sousa, N., Palha, J.A., and Marques, F. (2015). The choroid plexus transcriptome reveals changes in type I and II interferon responses in a mouse model of Alzheimer's disease. Brain Behav. Immun. *49*, 280–292.

7. Strominger, I., Elyahu, Y., Berner, O., Reckhow, J., Mittal, K., Nemirovsky, A., and Monsonego, A. (2018). The Choroid Plexus Functions as a Niche for T-Cell Stimulation Within the Central Nervous System. Front. Immunol. *9*, 1066.

8. Yin, C., Ackermann, S., Ma, Z., Mohanta, S.K., Zhang, C., Li, Y., Nietzsche, S., Westermann, M., Peng, L., Hu, D., et al. (2019). ApoE attenuates unresolvable inflammation by complex formation with activated C1q. Nat. Med. *25*, 496–506.

9. Reboldi, A., Coisne, C., Baumjohann, D., Benvenuto, F., Bottinelli, D., Lira, S., Uccelli, A., Lanzavecchia, A., Engelhardt, B., and Sallusto, F. (2009). C-C chemokine receptor 6-regulated entry of TH-17 cells into the CNS through the choroid plexus is required for the initiation of EAE. Nat. Immunol. *10*, 514–523.

10. Wang, L., Schuster, G.U., Hultenby, K., Zhang, Q., Andersson, S., and Gustafsson, J.-A. (2002). Liver X receptors in the central nervous system: from lipid homeostasis to neuronal degeneration. Proc. Natl. Acad. Sci. USA *99*, 13878–13883.

11. Spann, N.J., and Glass, C.K. (2013). Sterols and oxysterols in immune cell function. Nat. Immunol. *14*, 893–900.

12. Griffiths, W.J., and Wang, Y. (2020). Oxysterols as lipid mediators: Their biosynthetic genes, enzymes and metabolites. Prostaglandins Other Lipid Mediat. *147*, 106381.

13. Javitt, N.B. (2004). Oxysteroids: a new class of steroids with autocrine and paracrine functions. Trends Endocrinol. Metab. *15*, 393–397.

14. Lehmann, J.M., Kliewer, S.A., Moore, L.B., Smith-Oliver, T.A., Oliver, B.B., Su, J.L., Sundseth, S.S., Winegar, D.A., Blanchard, D.E., Spencer, T.A., and Willson, T.M. (1997). Activation of the nuclear receptor LXR by oxysterols defines a new hormone response pathway. J. Biol. Chem. *272*, 3137–3140.

15. Brown, J., Theisler, C., Silberman, S., Magnuson, D., Gottardi-Littell, N., Lee, J.M., Yager, D., Crowley, J., Sambamurti, K., Rahman, M.M., et al. (2004). Differential Expression of Cholesterol Hydroxylases in Alzheimer's Disease. J. Biol. Chem. *279*, 34674–34681.

16. Yutuc, E., Angelini, R., Baumert, M., Mast, N., Pikuleva, I., Newton, J., Clench, M.R., Skibinski, D.O.F., Howell, O.W., Wang, Y., and Griffiths, W.J. (2020). Localization of sterols and oxysterols in mouse brain reveals distinct spatial cholesterol metabolism. Proc. Natl. Acad. Sci. *117*, 5749–5760.

17. Uhlén, M., Fagerberg, L., Hallström, B.M., Lindskog, C., Oksvold, P., Mardinoglu, A., Sivertsson, Å., Kampf, C., Sjöstedt, E., Asplund, A., et al. (2015). Proteomics. Tissue-based map of the human proteome. Science *347*, 1260419.

18. Petrov, A.M., and Pikuleva, I.A. (2019). Cholesterol 24-Hydroxylation by CYP46A1: Benefits of Modulation for Brain Diseases. Neurotherapeutics *16*, 635–648.

19. Zeisel, A., Hochgerner, H., Lönnerberg, P., Johnsson, A., Memic, F., van der Zwan, J., Häring, M., Braun, E., Borm, L.E., La Manno, G., et al. (2018). Molecular Architecture of the Mouse Nervous System. Cell *174*, 999–1014.e22.

20. Lund, E.G., Xie, C., Kotti, T., Turley, S.D., Dietschy, J.M., and Russell, D.W. (2003). Knockout of the Cholesterol 24-Hydroxylase Gene in Mice Reveals a Brain-specific Mechanism of Cholesterol Turnover. J. Biol. Chem. *278*, 22980–22988.

21. Fujiyoshi, M., Ohtsuki, S., Hori, S., Tachikawa, M., and Terasaki, T. (2007). 24S-hydroxycholesterol induces cholesterol release from choroid plexus epithelial cells in an apical- and apoE isoform-dependent manner concomitantly with the induction of ABCA1 and ABCG1 expression. J. Neurochem. *100*, 968–978.

22. Dani, N., Herbst, R.H., McCabe, C., Green, G.S., Kaiser, K., Head, J.P., Cui, J., Shipley, F.B., Jang, A., Dionne, D., et al. (2021). A cellular and spatial map of the choroid plexus across brain ventricles and ages. Cell *184*, 3056–3074.e21.

23. Mast, N., El-Darzi, N., Petrov, A.M., Li, Y., and Pikuleva, I.A. (2020). CYP46A1-dependent and independent effects of efavirenz treatment. Brain Commun. *2*, fcaa180.

24. Oakley, H., Cole, S.L., Logan, S., Maus, E., Shao, P., Craft, J., Guillozet-Bongaarts, A., Ohno, M., Disterhoft, J., Van Eldik, L., et al. (2006). Intraneuronal beta-amyloid aggregates, neurodegeneration, and neuron loss in transgenic mice with five familial Alzheimer's disease mutations: potential factors in amyloid plaque formation. J. Neurosci. *26*, 10129–10140.

25. Hahn, O., Foltz, A.G., Atkins, M., Kedir, B., Moran-Losada, P., Guldner, I.H., Munson, C., Kern, F., Pálovics, R., Lu, N., et al. (2023). Atlas of the aging mouse brain reveals white matter as vulnerable foci. Cell *186*, 4117–4133.e22.

26. Liu, Y.-H., Chen, Y., Wang, Q.-H., Wang, L.-R., Jiang, L., Yang, Y., Chen, X., Li, Y., Cen, Y., Xu, C., et al. (2022). One-Year Trajectory of Cognitive Changes in Older Survivors of COVID-19 in Wuhan, China: A Longitudinal Cohort Study. JAMA Neurol. *79*, 509–517.

27. Hampshire, A., Trender, W., Chamberlain, S.R., Jolly, A.E., Grant, J.E., Patrick, F., Mazibuko, N., Williams, S.C., Barnby, J.M., Hellyer, P., and Mehta, M.A. (2021). Cognitive deficits in people who have recovered from COVID-19. EClinicalMedicine *39*, 101044.

28. Bogdanovic, N., Bretillon, L., Lund, E.G., Diczfalusy, U., Lannfelt, L., Winblad, B., Russell, D.W., and Björkhem, I. (2001). On the turnover of brain cholesterol in patients with Alzheimer's disease. Abnormal induction of the cholesterol-catabolic enzyme CYP46 in glial cells. Neurosci. Lett. *314*, 45–48.

29. Jarius, S., Pache, F., Körtvelyessy, P., Jelčić, I., Stettner, M., Franciotta, D., Keller, E., Neumann, B., Ringelstein, M., Senel, M., et al. (2022). Cerebrospinal fluid findings in COVID-19: a multicenter study of 150 lumbar punctures in 127 patients. J. Neuroinflammation *19*, 19.

30. Stopa, E.G., Tanis, K.Q., Miller, M.C., Nikonova, E.V., Podtelezhnikov, A.A., Finney, E.M., Stone, D.J., Camargo, L.M., Parker, L., Verma, A., et al. (2018). Comparative transcriptomics of choroid plexus in Alzheimer's disease, frontotemporal dementia and Huntington's disease: implications for CSF homeostasis. Fluids Barriers CNS *15*, 18.

31. Kant, S., Stopa, E.G., Johanson, C.E., Baird, A., and Silverberg, G.D. (2018). Choroid plexus genes for CSF production and brain homeostasis are altered in Alzheimer's disease. Fluids Barriers CNS *15*, 34.

32. Fullard, J.F., Lee, H.C., Voloudakis, G., Suo, S., Javidfar, B., Shao, Z., Peter, C., Zhang, W., Jiang, S., Corvelo, A., et al. (2021). Single-nucleus transcriptome analysis of human brain immune response in patients with severe COVID-19. Genome Med. *13*, 118.

33. Pellegrini, L., Albecka, A., Mallery, D.L., Kellner, M.J., Paul, D., Carter, A.P., James, L.C., and Lancaster, M.A. (2020). SARS-CoV-2 Infects the Brain Choroid Plexus and Disrupts the Blood-CSF Barrier in Human Brain Organoids. Cell Stem Cell *27*, 951–961.e5.

34. Jacob, F., Pather, S.R., Huang, W.-K., Zhang, F., Wong, S.Z.H., Zhou, H., Cubitt, B., Fan, W., Chen, C.Z., Xu, M., et al. (2020). Human Pluripotent Stem Cell-Derived Neural Cells and Brain Organoids Reveal SARS-CoV-2 Neurotropism Predominates in Choroid Plexus Epithelium. Cell Stem Cell *27*, 937–950.e9.

35. Kunis, G., Baruch, K., Rosenzweig, N., Kertser, A., Miller, O., Berkutzki, T., and Schwartz, M. (2013). IFN-γ-dependent activation of the brain's choroid plexus for CNS immune surveillance and repair. Brain *136*, 3427–3440.

36. Gamba, P., Giannelli, S., Staurenghi, E., Testa, G., Sottero, B., Biasi, F., Poli, G., and Leonarduzzi, G. (2021). The Controversial Role of 24-S-Hydroxycholesterol in Alzheimer's Disease. Antioxidants *10*, 740.

37. Villeda, S.A., Luo, J., Mosher, K.I., Zou, B., Britschgi, M., Bieri, G., Stan, T.M., Fainberg, N., Ding, Z., Eggel, A., et al. (2011). The ageing systemic milieu negatively regulates neurogenesis and cognitive function. Nature *477*, 90–94.

38. Fernández-Castañeda, A., Lu, P., Geraghty, A.C., Song, E., Lee, M.H., Wood, J., O'Dea, M.R., Dutton, S., Shamardani, K., Nwangwu, K., et al. (2022). Mild respiratory COVID can cause multi-lineage neural cell and myelin dysregulation. Cell *185*, 2452–2468.e16.

39. Blank, T., Detje, C.N., Spieß, A., Hagemeyer, N., Brendecke, S.M., Wolfart, J., Staszewski, O., Zöller, T., Papageorgiou, I., Schneider, J., et al. (2016). Brain Endothelial- and Epithelial-Specific Interferon Receptor Chain 1 Drives Virus-Induced Sickness Behavior and Cognitive Impairment. Immunity *44*, 901–912.

40. Rodríguez-Lorenzo, S., Ferreira Francisco, D.M., Vos, R., van het Hof, B., Rijnsburger, M., Schroten, H., Ishikawa, H., Beaino, W., Bruggmann, R., Kooij, G., and de Vries, H.E. (2020). Altered secretory and neuroprotective function of the choroid plexus in progressive multiple sclerosis. Acta Neuropathol. Commun. *8*, 35.

41. Kim, S., Hwang, Y., Lee, D., and Webster, M.J. (2016). Transcriptome sequencing of the choroid plexus in schizophrenia. Transl. Psychiatry *6*, e964.

42. Van Hoecke, L., Van Cauwenberghe, C., Dominko, K., Van Imschoot, G., Van Wonterghem, E., Castelein, J., Xie, J., Claeys, W., Vandendriessche, C., Kremer, A., et al. (2021). Involvement of the Choroid Plexus in the Pathogenesis of Niemann-Pick Disease Type C. Front. Cell. Neurosci. *15*, 757482.

43. Zhao, N., Ren, Y., Yamazaki, Y., Qiao, W., Li, F., Felton, L.M., Mahmoudiandehkordi, S., Kueider-Paisley, A., Sonoustoun, B., Arnold, M., et al. (2020). Alzheimer's Risk Factors Age, APOE Genotype, and Sex Drive Distinct Molecular Pathways. Neuron *106*, 727–742. https://doi.org/10.1016/J.NEURON.2020.02.034/ATTACHMENT/583D0517-42B6-4C4A-8A4A-735931261C4E/MMC5.XLSX.

44. Vanni, S., Moda, F., Zattoni, M., Bistaffa, E., De Cecco, E., Rossi, M., Giaccone, G., Tagliavini, F., Haïk, S., Deslys, J.P., et al. (2017). Differential overexpression of SERPINA3 in human prion diseases. Sci. Rep. *7*, 15637.

45. Hayden, M.S., and Ghosh, S. (2014). Regulation of NF-κB by TNF family cytokines. Semin. Immunol. *26*, 253–266.

46. Baruch, K., Kertser, A., Porat, Z., and Schwartz, M. (2015). Cerebral nitric oxide represses choroid plexus NFkappaB-dependent gateway activity for leukocyte trafficking. EMBO J. *34*, 1816–1828.

47. Mast, N., Li, Y., Linger, M., Clark, M., Wiseman, J., and Pikuleva, I.A. (2014). Pharmacologic stimulation of cytochrome P450 46A1 and cerebral cholesterol turnover in mice. J. Biol. Chem. *289*, 3529–3538.

48. Mast, N., Verwilst, P., Wilkey, C.J., Guengerich, F.P., and Pikuleva, I.A. (2020). In Vitro Activation of Cytochrome P450 46A1 (CYP46A1) by Efavirenz-Related Compounds. J. Med. Chem. *63*, 6477–6488.

49. Dvir-Szternfeld, R., Castellani, G., Arad, M., Cahalon, L., Colaiuta, S.P., Keren-Shaul, H., Croese, T., Burgaletto, C., Baruch, K., Ulland, T., et al. (2022). Alzheimer's disease modification mediated by bone marrow-derived macrophages via a TREM2-independent pathway in mouse model of amyloidosis. Nat. Aging *2*, 60–73.

50. Suzzi, S., Croese, T., Ravid, A., Gold, O., Clark, A.R., Medina, S., Kitsberg, D., Adam, M., Vernon, K.A., Kohnert, E., et al. (2023). N-acetylneuraminic acid links immune exhaustion and accelerated memory deficit in diet-induced obese Alzheimer's disease mouse model. Nat. Commun. *14*, 1293.

51. Smith, L.K., He, Y., Park, J.S., Bieri, G., Snethlage, C.E., Lin, K., Gontier, G., Wabl, R., Plambeck, K.E., Udeochu, J., et al. (2015). β2-microglobulin is a systemic pro-aging factor that impairs cognitive function and neurogenesis. Nat. Med. *21*, 932–937.

52. Allred, M.G., Chimenti, M.S., Ciecko, A.E., Chen, Y.G., and Lieberman, S.M. (2021). Characterization of type I interferon-associated chemokines and cytokines in lacrimal glands of nonobese diabetic mice. Int. J. Mol. Sci. *22*, 3767.

53. Rosenzweig, N., Dvir-Szternfeld, R., Tsitsou-Kampeli, A., Keren-Shaul, H., Ben-Yehuda, H., Weill-Raynal, P., Cahalon, L., Kertser, A., Baruch, K., Amit, I., et al. (2019). PD-1/PD-L1 checkpoint blockade harnesses monocyte-derived macrophages to combat cognitive impairment in a tauopathy mouse model. Nat. Commun. *10*, 465.

54. Griciuc, A., Patel, S., Federico, A.N., Choi, S.H., Innes, B.J., Oram, M.K., Cereghetti, G., McGinty, D., Anselmo, A., Sadreyev, R.I., et al. (2019). TREM2 Acts Downstream of CD33 in Modulating Microglial Pathology in Alzheimer's Disease. Neuron *103*, 820–835.e7.

55. Udeochu, J.C., Amin, S., Huang, Y., Fan, L., Torres, E.R.S., Carling, G.K., Liu, B., McGurran, H., Coronas-Samano, G., Kauwe, G., et al. (2023). Tau activation of microglial cGAS–IFN reduces MEF2C-mediated cognitive resilience. Nat. Neurosci. *26*, 737–750.

56. Burlot, M.-A., Braudeau, J., Michaelsen-Preusse, K., Potier, B., Ayciriex, S., Varin, J., Gautier, B., Djelti, F., Audrain, M., Dauphinot, L., et al. (2015). Cholesterol 24-hydroxylase defect is implicated in memory impairments associated with Alzheimer-like Tau pathology. Hum. Mol. Genet. *24*, 5965–5976.

57. Boussicault, L., Alves, S., Lamazière, A., Planques, A., Heck, N., Moumné, L., Despres, G., Bolte, S., Hu, A., Pagès, C., et al. (2016). CYP46A1, the rate-limiting enzyme for cholesterol degradation, is neuroprotective in Huntington's disease. Brain *139*, 953–970.

58. Nóbrega, C., Mendonça, L., Marcelo, A., Lamazière, A., Tomé, S., Despres, G., Matos, C.A., Mechmet, F., Langui, D., den Dunnen, W., et al. (2019). Restoring brain cholesterol turnover improves autophagy and has therapeutic potential in mouse models of spinocerebellar ataxia. Acta Neuropathol. *138*, 837–858.

59. Ali, T., Hannaoui, S., Nemani, S., Tahir, W., Zemlyankina, I., Cherry, P., Shim, S.Y., Sim, V., Schaetzl, H.M., and Gilch, S. (2021). Oral administration of repurposed drug targeting Cyp46A1 increases survival times of prion infected mice. Acta Neuropathol. Commun. *9*, 58.

60. Hu, W.T., Howell, J.C., Ozturk, T., Gangishetti, U., Kollhoff, A.L., Hatcher-Martin, J.M., Anderson, A.M., and Tyor, W.R. (2019). CSF Cytokines in Aging, Multiple Sclerosis, and Dementia. Front. Immunol. *10*, 480.

61. Pilotto, A., Masciocchi, S., Volonghi, I., De Giuli, V., Caprioli, F., Mariotto, S., Ferrari, S., Bozzetti, S., Imarisio, A., Risi, B., et al. (2021). Severe Acute Respiratory Syndrome Coronavirus 2 (SARS-CoV-2) Encephalitis Is a Cytokine Release Syndrome: Evidences From Cerebrospinal Fluid Analyses. Clin. Infect. Dis. *73*, e3019–e3026.

62. Pascoal, T.A., Benedet, A.L., Ashton, N.J., Kang, M.S., Therriault, J., Chamoun, M., Savard, M., Lussier, F.Z., Tissot, C., Karikari, T.K., et al. (2021). Microglial activation and tau propagate jointly across Braak stages. Nat. Med. *27*, 1592–1599.

63. Mast, N., Saadane, A., Valencia-Olvera, A., Constans, J., Maxfield, E., Arakawa, H., Li, Y., Landreth, G., and Pikuleva, I.A. (2017). Cholesterol-metabolizing enzyme cytochrome P450 46A1 as a pharmacologic target for Alzheimer's disease. Neuropharmacology *123*, 465–476.

64. Petrov, A.M., Lam, M., Mast, N., Moon, J., Li, Y., Maxfield, E., and Pikuleva, I.A. (2019). CYP46A1 Activation by Efavirenz Leads to Behavioral Improvement without Significant Changes in Amyloid Plaque Load in the Brain of 5XFAD Mice. Neurotherapeutics *16*, 710–724.

65. Testa, G., Staurenghi, E., Giannelli, S., Gargiulo, S., Guglielmotto, M., Tabaton, M., Tamagno, E., Gamba, P., and Leonarduzzi, G. (2018). A silver lining for 24-hydroxycholesterol in Alzheimer's disease: The involvement of the neuroprotective enzyme sirtuin 1. Redox Biol. *17*, 423–431.

66. Pikuleva, I.A., and Cartier, N. (2021). Cholesterol Hydroxylating Cytochrome P450 46A1: From Mechanisms of Action to Clinical Applications. Front. Aging Neurosci. *13*, 696778.

67. Moutinho, M., Nunes, M.J., Gomes, A.Q., Gama, M.J., Cedazo-Minguez, A., Rodrigues, C.M.P., Björkhem, I., Rodrigues, E., Björkhem, I., and Rodrigues, E. (2015). Cholesterol 24S-Hydroxylase Overexpression Inhibits the Liver X Receptor (LXR) Pathway by Activating Small Guanosine Triphosphate-Binding Proteins (sGTPases) in Neuronal Cells. Mol. Neurobiol. *51*, 1489–1503.

68. Chen, X., He, Y., Tian, Y., Wang, Y., Wu, Z., Lan, T., Wang, H., Cheng, K., and Xie, P. (2020). Different Serotypes of Adeno-Associated Virus Vector- and Lentivirus-Mediated Tropism in Choroid Plexus by Intracerebroventricular Delivery. Hum. Gene Ther. *31*, 440–447.

69. Jang, A., and Lehtinen, M.K. (2022). Experimental approaches for manipulating choroid plexus epithelial cells. Fluids Barriers CNS *19*, 36.

70. Johnston, S., Parylak, S.L., Kim, S., Mac, N., Lim, C., Gallina, I., Bloyd, C., Newberry, A., Saavedra, C.D., Novak, O., et al. (2021). AAV ablates neurogenesis in the adult murine hippocampus. Elife *10*, e59291.

71. Chan, Y.K., Wang, S.K., Chu, C.J., Copland, D.A., Letizia, A.J., Costa Verdera, H., Chiang, J.J., Sethi, M., Wang, M.K., Neidermyer, W.J., et al. (2021). Engineering adeno-associated viral vectors to evade innate immune and inflammatory responses. Sci. Transl. Med. *13*, eabd3438.

72. Love, M.I., Huber, W., and Anders, S. (2014). Moderated estimation of fold change and dispersion for RNA-seq data with DESeq2. Genome Biol. *15*, 550.

73. Zhu, A., Ibrahim, J.G., and Love, M.I. (2019). Heavy-tailed prior distributions for sequence count data: removing the noise and preserving large differences. Bioinformatics *35*, 2084–2092.

74. Hao, Y., Hao, S., Andersen-Nissen, E., Mauck, W.M., 3rd, Zheng, S., Butler, A., Lee, M.J., Wilk, A.J., Darby, C., Zager, M., et al. (2021). Integrated analysis of multimodal single-cell data. Cell *184*, 3573–3587.e29.

75. Schneider, C.A., Rasband, W.S., and Eliceiri, K.W. (2012). NIH Image to ImageJ: 25 years of image analysis. Nat. Methods *9*, 671–675.

76. Campbell, J.H., Foster, C.M., Vishnivetskaya, T., Campbell, A.G., Yang, Z.K., Wymore, A., Palumbo, A.V., Chesler, E.J., and Podar, M. (2012). Host genetic and environmental effects on mouse intestinal microbiota. ISME J. *6*, 2033–2044.

77. Livak, K.J., and Schmittgen, T.D. (2001). Analysis of relative gene expression data using real-time quantitative PCR and the 2(-Delta Delta C(T)) Method. Methods *25*, 402–408.

78. Zincarelli, C., Soltys, S., Rengo, G., and Rabinowitz, J.E. (2008). Analysis of AAV serotypes 1-9 mediated gene expression and tropism in mice after systemic injection. Mol. Ther. *16*, 1073–1080.

79. Zolotukhin, S., Byrne, B.J., Mason, E., Zolotukhin, I., Potter, M., Chesnut, K., Summerford, C., Samulski, R.J., and Muzyczka, N. (1999). Recombinant adeno-associated virus purification using novel methods improves infectious titer and yield. Gene Ther. *6*, 973–985.

80. Levy, D., Adamovich, Y., Reuven, N., and Shaul, Y. (2007). The Yes-associated protein 1 stabilizes p73 by preventing Itch-mediated ubiquitination of p73. Cell Death Differ. *14*, 743–751.

81. Bevins, R.A., and Besheer, J. (2006). Object recognition in rats and mice: a one-trial non-matching-to-sample learning task to study "recognition memory". Nat. Protoc. *1*, 1306–1311.

82. Susaki, E.A., Tainaka, K., Perrin, D., Yukinaga, H., Kuno, A., and Ueda, H.R. (2015). Advanced CUBIC protocols for whole-brain and whole-body clearing and imaging. Nat. Protoc. *10*, 1709–1727.

83. Keren-Shaul, H., Kenigsberg, E., Jaitin, D.A., David, E., Paul, F., Tanay, A., and Amit, I. (2019). MARS-seq2.0: an experimental and analytical pipeline for indexed sorting combined with single-cell RNA sequencing. Nat. Protoc. *14*, 1841–1862.

84. Kim, D., Langmead, B., and Salzberg, S.L. (2015). HISAT: a fast spliced aligner with low memory requirements. Nat. Methods *12*, 357–360.

85. Zhou, Y., Zhou, B., Pache, L., Chang, M., Khodabakhshi, A.H., Tanaseichuk, O., Benner, C., and Chanda, S.K. (2019). Metascape provides a biologist-oriented resource for the analysis of systems-level datasets. Nat. Commun. *10*, 1523.

86. Irizarry, R.A., Hobbs, B., Collin, F., Beazer-Barclay, Y.D., Antonellis, K.J., Scherf, U., and Speed, T.P. (2003). Exploration, normalization, and summaries of high density oligonucleotide array probe level data. Biostatistics *4*, 249–264.

87. Finak, G., McDavid, A., Yajima, M., Deng, J., Gersuk, V., Shalek, A.K., Slichter, C.K., Miller, H.W., McElrath, M.J., Prlic, M., et al. (2015). MAST: a flexible statistical framework for assessing transcriptional changes and characterizing heterogeneity in single-cell RNA sequencing data. Genome Biol. *16*, 278.

88. Han, H., Cho, J.W., Lee, S., Yun, A., Kim, H., Bae, D., Yang, S., Kim, C.Y., Lee, M., Kim, E., et al. (2018). TRRUST v2: An expanded reference database of human and mouse transcriptional regulatory interactions. Nucleic Acids Res. *46*, D380–D386.

89. Bader, G.D., and Hogue, C.W.V.((2003). An automated method for finding molecular complexes in large protein interaction networks. BMC Bioinf. *4*, 2.

STAR★METHODS

KEY RESOURCES TABLE

REAGENT or RESOURCE	SOURCE	IDENTIFIER
Antibodies		
anti-mouse β-actin	Sigma	RRID:AB_476697
rabbit anti-mouse CYP46A1	Proteintech	RRID:AB_2090661
rabbit anti-mouse cleaved caspase 3	Cell Signaling	RRID:AB_2341188
rabbit anti-mouse claudin 1	ThermoFisher	AB_2533916
rabbit anti-mouse/human CYP46A1	Proteintech	RRID:AB_2090661
rabbit anti-GFAP	Dako	RRID:AB_10013382
rabbit ant-IBA1	Wako	RRID:AB_839504
rat anti-mouse CD31	BD Biosciences	RRID:AB_394816
rabbit anti-mouse/human CYP46A1	Proteintech	RRID:AB_2090661
mouse anti-mouse ZO-1	Invitrogen	AB_2533147
anti-mouse CD45 APC, clone 30F-11	eBioscience	AB_469392
anti-mouse CD11 b PE, clone M1/70	eBioscience	AB_2734869
Bacterial and virus strains		
rAAV1	This paper	N/A
Biological samples		
Postmortem human choroid plexus, paraffin-embedded	Oxford Brain Bank (formerly known as the Thomas Willis Oxford Brain Collection, TWOBC)	https://www.hra.nhs.uk/planning-and-improving-research/application-summaries/research-summaries/the-oxford-brain-bank/
Postmortem human choroid plexus, paraffin-embedded	Southwest Dementia Brain Bank (SWDBB)	https://www.alzheimers-brace.org/the-south-west-dementia-brain-bank/
Chemicals, peptides, and recombinant proteins		
Recombinant Human TNF-α	PeproTech	CAT# 300-01A
Neutralizing antibodies to TNFRs	BioLegend	CAT# 112902
24-OH	Sigma	CAS: 474-73-7
efavirenz	Universal biologicals	CAT# CS-2154
water-soluble cholesterol	Sigma	Product# C4951
Critical commercial assays		
Quick-RNA MicroPrep kit	Zymo Research	CAT# R1051
Qiagen Plasmid Plus Midi kit	Qiagen	CAT# 12943
human Aβ42 Ultrasensitive ELISA Kit	Invitrogen	CAT# KHB3544
Pierce BCA Protein Assay Kit	Thermo Scientific™	CAT# 23225
Dynabeads mRNA purification kit	Invitrogen	CAT# 61006
Deposited data		
Bulk RNA-seq data of primary mouse CP cell cultures	This paper	GEO: GSE200318
Single-nucleus RNA-seq data of mouse CP	Dani et al.[22]	GEO: GSE168704
Single-nucleus RNA-seq data of postmortem human CP and cortex	Yang et al.[3]	GEO: GSE159812
Transcriptome-wide Affymetrix microarrays of human CP	Stopa et al.[30]	GEO: GSE110226
High throughput sequencing of human CP	Rodríguez-Lorenzo et al.[40]	GEO: GSE137619
Analysis of bulk RNA-seq data of primary mouse CP cell cultures	This paper	https://doi.org/10.5281/zenodo.8251509
Analysis of mouse and human CP transcriptome data	This paper	https://doi.org/10.5281/zenodo.8249889

(*Continued on next page*)

Continued

REAGENT or RESOURCE	SOURCE	IDENTIFIER
Experimental models: Cell lines		
HEK293T	ATCC	CAT# CRL-3216
Experimental models: Organisms/strains		
5xFAD line Tg6799 C57/BL6-SJL	Jackson Laboratory	N/A
C57BL/6JOlaHsd	ENVIGO	N/A
Oligonucleotides		
See Table S4 for primer sequences		N/A
Recombinant DNA		
pAAV-EF1a-mCyp46a1	This paper	N/A
pAAV-EF1a -GFP	This paper	N/A
Software and algorithms		
DESeq2 (version 1.26 and 1.16.1)	Love et al.[72]	N/A
apeglm (version 1.8)	Zhu et al.[73]	N/A
Seurat package version 4.2.0	Hao et al.[74]	N/A
Partek® Genomics Suite®, version 7.19.1125	https://www.partek.com/partek-genomics-suite/	N/A
Ethovision XT 11 software	Noldus	N/A
NIS-Elements	F3, Nikon	N/A
LSM880	Zeiss	N/A
ImageJ	Shneider et al.[75]	N/A
Spark microplate reader	Tecan	N/A

RESOURCE AVAILABILITY

Lead contact

Further information and requests for resources and reagents should be directed to and will be fulfilled by the lead contact, Prof. Michal Schwartz (michal.schwartz@weizmann.ac.il).

Materials availability

AAV_mCYP46A1 or AAV_GFP plasmids generated in this study are available from the lead contact without restriction. Further information and requests for resources and reagents should be directed to and will be fulfilled by the lead contact, Prof. Michal Schwartz (michal.schwartz@weizmann.ac.il).

Data and code availability

Bulk RNA-seq data of primary mouse CP cell cultures have been deposited to GEO and are publicly available; the related accession number (GEO: GSE200318) is listed in the Key resources table. For the published datasets analyzed in this paper, the accession numbers are listed in the Key resources table. The working codes used for the analyses in this paper have been deposited to Zenodo and are publicly available; the related DOIs (https://doi.org/10.5281/zenodo.8251509, https://doi.org/10.5281/zenodo.8249889) are listed in the Key resources table. Any additional information required to reanalyze the data reported in this paper is available from the lead contact upon request.

EXPERIMENTAL MODEL AND STUDY PARTICIPANT DETAILS

Animal models

All experiments detailed herein complied with the regulations formulated by the Institutional Animal Care and Use Committee (IACUC) of the Weizmann Institute of Science (application numbers: 04910522-1, 01590221-2, 00610120-3, 17501019-1). Female and male mice were bred and maintained by the Animal Breeding Center of the Weizmann Institute of Science. Housing conditions were: 12 h dark/light cycle, temperature 22 °C, humidity 30–70%. Heterozygous 5xFAD transgenic mice (on a C57/BL6-SJL background) that overexpress familial AD mutant forms of human APP (the Swedish mutation, K670N/M671L; the Florida mutation, I716V; and the London mutation, V717I) and PS1 (M146L/L286V) transgenes under the transcriptional control of the neuron-specific mouse *Thy1* promoter[24] (5xFAD line Tg6799; the Jackson Laboratory) and wildtype (WT) control littermates were used. To avoid gut microbiota-related cage effects due to coprophagia,[76] mice of different genotypes and treatments were housed together. Littermates of the

same sex were randomly assigned to experimental groups. Mice allocated for behavioral studies were switched to a 12 h reversed dark/light cycle at least 7 days prior to the start of the experiments, and maintained in the same regimen until the experimental endpoint (9–12 months of age). Genotyping was performed by PCR analysis of ear-punch DNA. For primary mouse CP cultures and mouse CP organ cultures, adult mice, of both sexes, with a wild-type background (C57/BL6-SJL or C57/BL6 strain) and age between 3 and 10 months were used.

Postmortem human CP samples

Paraffin-embedded sections of postmortem Alzheimer's disease (AD) patients and age-matched individuals with no neurologic history were obtained from the Oxford Brain Bank (formerly known as the Thomas Willis Oxford Brain Collection, TWOBC) and the Southwest Dementia Brain Bank (SWDBB) with appropriate consent and Ethics Committee approval (TW220). All samples were approved by the Institutional Review Board (IRB) of the Weizmann Institute of Science (ID: 1192-1). Sample and patient characteristics are reported in Table S1, *Population characteristics*.

METHOD DETAILS

Mouse tissue collection

Anesthetized mice were transcardially perfused with phosphate buffered saline (PBS). For CP cultures, mice were immersed in 70% ethanol immediately after perfusion, and CP tissue from lateral, third, and fourth ventricles were dissected under a sterile hood, and processed fresh. For qRT-PCR, hippocampus and cortex from one hemisphere were snap-frozen in liquid nitrogen, and CP tissue from all ventricles was snap-frozen in dry ice. Note: for *B2m* and *Ccl12* assessment at the CP, in one out of the three experiments, CP tissue from all ventricles except the left lateral ventricle were pooled. For Western blot, CP tissue from all ventricles, cortices, hippocampi, and spleens were excised and snap-frozen in dry-ice.

RNA purification and cDNA synthesis

Total RNA from excised tissues (CP, hippocampus, cortex), primary CP epithelial cultures, or mouse CP organ cultures was extracted with the Quick-RNA MicroPrep kit (Zymo Research) for CP tissue and with Rneasy Mini kit (Qiagen) for hippocampi and cortices, and mRNA (up to 1 μg) was reverse-transcribed to cDNA using a High Capacity cDNA Reverse Transcription Kit (Applied Biosystems).

qRT-PCR analysis

The expression of specific mRNAs was assayed using fluorescence-based quantitative real-time PCR (qRT-PCR). qRT-PCR reactions were performed using Fast-SYBR PCR Master Mix (Applied Biosystems). Quantification reactions were performed in duplicate for each sample using the $2^{-\Delta\Delta Ct}$ method.[77] Peptidylprolyl isomerase A (*Ppia*) and hypoxanthine guanine phosphoribosyl transferase (*Hprt*) were used as reference genes for the CP and brain parenchyma, respectively. The amplification cycles were 95 °C for 5 s, 60 °C for 20 s, and 72 °C for 15 s. At the end of the assay, a melting curve was constructed to evaluate the specificity of the reaction. All qRT-PCR reactions were performed and analyzed using StepOne software V2.2.2 (Applied Biosystems). The primers used are listed in Table S4. To determine the expression levels of *Il1b* and *Tnfa* in hippocampus and cortex, cDNA was pre-amplified using the PreAmp Master Mix kit (Applied Biosystems) according to the manufacturer's protocol to increase qRT-PCR sensitivity. TaqMan Assays-on-Demand probes used are listed in Table S4.

Primary mouse CP cell cultures

Primary mouse CP cell cultures were produced as previously described.[35] Briefly, CP tissues were excised following perfusion with PBS and kept on ice in 0.25% trypsin (Sigma), then digested at 37°C under agitation, and manually dissociated into a single-cell suspension. All wells were seeded with cells from the same pooled suspension. Approximately 2×10^5 cells were cultured in 24-well plates in Dulbecco's modified Eagle's medium (DMEM)/Ham's F12 (Invitrogen) supplemented with 10% fetal calf serum (FCS), 1 mM L-glutamine, 1 mM sodium pyruvate, penicillin (100 U/mL), streptomycin (100 mg/mL), insulin (5 μg/mL), 20 μM arabinosylcytosine, sodium selenite (5 ng/mL), and epidermal growth factor (10 ng/mL). All reagents were from Sigma. The medium was refreshed every 24 h, and after 72 h, 24-OH (0.1, 1 or 10 μM from a 3 mg/mL stock in DMSO; Sigma) or DMSO control was added for an incubation time of 12 or 24 h. TNF-α (100 ng/mL; PeproTech) was added after 24 h of cell culture and for an incubation time of 24 h, with medium-only controls employed, as previously described.[35] Neutralizing antibodies to TNFR1 or TNFR2 (20 μg/mL, BioLegend) were added 1 h before the addition of TNF-α (100 ng/mL), as previously described.[35] RNA was isolated using the Quick-RNA MicroPrep kit (Zymo Research) according to the manufacturer's protocol.

Mouse CP organ cultures

For all experiments involving whole mouse CP organ cultures, the same culture medium as for primary mouse CP cell cultures (STAR Methods, *Primary mouse CP cell cultures*) was used. For experiments involving AAV infection or efavirenz stimulation, cultures were maintained and treated in medium supplemented with 40 μM water-soluble cholesterol (Sigma). For each mouse, CP tissue from one of the two lateral ventricles was excised after perfusion with PBS, and was cultured in a 24-well plate in 1 mL of medium. After overnight acclimatization to the medium, CP explants were stimulated based on the experimental design as follows. For stimulation with

24-OH, CP explants from left lateral ventricles were individually incubated in 500 μL of 0.1, 1 or 10 μM 24-OH or DMSO control for 24 h. For AAV infection followed by stimulation with TNF-α, CP explants from left lateral ventricles were individually incubated in 300 μL of medium containing 0.2 × 10^9 vg of AAV1_mCYP46A1 or AAV1_GFP control virus for 8 h. Subsequently, virus-containing medium was removed, and CP explants washed and then left to acclimatize in medium for 24 h, after which the medium was replaced and cultures were incubated for another 16 h. After a total of 40 h following virus removal, 500 μL of 20 ng/mL TNF-α (PeproTech) with 0.1% bovine serum albumin (BSA) or BSA-only control were added for 24 h. For stimulation with efavirenz (Universal biologicals) followed by stimulation with TNF-α, CP explants from right lateral ventricles were individually incubated in 500 μL of 20 μM or 40 μM of efavirenz (from a 38 mg/mL stock in DMSO) or DMSO control for 24 h. The efavirenz concentrations were chosen based on a previous study with purified recombinant human CYP46A1 (ref. [48]). Subsequently, treatment was removed, and CP explants were washed and incubated in 500 μL of 20 ng/mL TNF-α with 0.1% BSA or BSA-only control for an additional 24 h. At the end of each experiment, CP tissue was collected and snap-frozen in dry ice.

Viral plasmid cloning and AAV1 preparation

Murine *Cyp46a1* (*mCyp46a1*)-cDNA was cloned into a pAAV-EF1a-GFP vector using the primer pair: 5′-ATATCCATGGCGCCGAC CACGAGCCATGA-3′ (forward), 5′-ATATTGTACAACCTTACCCAGGGCTCAGCA-3′ (reverse) and replacing the GFP cassette between the NcoI and BsrGI restriction sites (enzymes from New England Biolabs). The cloning was performed according to the i-pfu PCR PreMix protocol (iNtRON Biotechnology DR) with modified annealing temperature of 70°C and addition of 5% DMSO to the PCR mix. The plasmids were purified with Qiagen Plasmid Plus Midi kit (Qiagen). To prepare AAVs, low-passage HEK293T (ATCC, catalog no. CRL-3216) were maintained at 37°C with 5% CO_2 in Dulbecco's modified Eagle's medium supplemented with 10% fetal bovine serum. To produce rAAV1, a triple co-transfection procedure was used to introduce a rAAV vector plasmid (pAAV-EF1a-mCyp46a1 or pAAV-EF1a -GFP) together with pXR1, an AAV1 helper plasmid carrying AAV *rep* and *cap* genes, and pXX6-80, an Ad helper plasmid, at a 1:1:1 M ratio.[78] Briefly, HEK293T cells were transfected using poly-ethylenimine (PEI, linear, MW 25,000; Polysciences), and medium was replaced 12 h post-transfection. Cells were harvested 72 h post-transfection, subjected to three rounds of freeze-thawing, and then digested with 100 U/mL benzonase (EMD Millipore) at 37°C for 1 h. Viral vectors were purified by iodixanol (Sigma) gradient ultracentrifugation[79] followed by further concentration using Amicon ultra-15 100K (100,000-molecular-weight cut-off; Millipore) and washed with phosphate-buffered saline (PBS). Two separate AAV1 viral preparations were used. Final concentration of rAAV1 particles was either 1.44 × 10^{10} vg/μL or 5.59 × 10^9 vg/μL (AAV-EF1a-mCyp46a1) and either 5.02 × 10^9 vg/μL or 2.92 × 10^9 vg/μL (pAAV- EF1a -GFP).

AAV intracerebroventricular injections

Virus was administered to the mice bilaterally intracerebroventricularly (0.4 mm posterior to the bregma, ±1.0 mm lateral to the midline, and 2.3 mm in depth from the skull surface). For each hemisphere, mice received 2.0 × 10^9 vg of AAV virus at a concentration of 1.0 × 10^9 vg/μL.

Exclusion criteria for AAV_mCYP46A1 mice

Among the total twenty-three AAV_mCYP46A1 mice analyzed, four mice displayed relatively low expression levels of *Cyp46a1* at the CP (log_2fc < 2.000) and were thus excluded from further analyses. Among the remaining nineteen AAV_mCYP46A1 mice, four showed a high expression of *Cyp46a1* in the hippocampus in addition to the high expression in the CP (log_2fc>1.000), and were thus also excluded from further analyses. Altogether, out of the initial twenty-three AAV_mCYP46A1 mice, for further analyses we retained fifteen mice (AAV_mCYP46A1^{in}). Cortical *Cyp46a1* expression measured in some of the AAV_mCYP46A1^{in} mice revealed significant but only marginal overexpression (log_2fc < 1.000).

Western blot

Frozen tissues were homogenized in radioimmunoprecipitation (RIPA)-buffer containing protease inhibitor (APExBIO) and phosphatase inhibitor (Sigma) using a glass pestle and mortar. HEK293 were harvested with cold PBS, centrifuged for 5 min at 3,500 rpm at 4°C, and resuspended in RIPA. Tissue homogenates and cell suspension were incubated for 10 min on ice. During the incubation period, tissue homogenates were sonicated for 2 min at 10 s intervals at an amplitude of 60%. Tissue homogenates and cell solutions were centrifuged at 4°C for 15 min, and the supernatant was mixed with Laemmli buffer. SDS-PAGE and immunoblotting were performed as described previously.[80] Blots were incubated overnight with either mouse anti-mouse β-actin (1:1,000; Sigma, A2228) or rabbit anti-mouse CYP46A1 (1:500; Proteintech, 12486-1-AP) overnight, and then for 1 h with horseradish peroxidase-conjugated anti-mouse or rabbit antibody (1:10,000; Jackson ImmunoResearch). EZ-ECL kit (Biological Industries) was used according to the manufacturer's instructions, before recording with ImageQuant LAS 4000 (GE Healthcare).

Novel object recognition (NOR) assay

A previously published protocol[81] was modified as follows. Mice were handled daily for 7 days prior to the experiment. The experiment spanned 2 days and included 3 trials: habituation trial (day 1, 20 min session in the empty arena); familiarization trial (day 2, 10 min session in the arena with two identical objects located in opposite corners of the floor, approximately 9 cm from the walls on each side); test trial (60 min after familiarization, 6 min session in the arena with one of the objects replaced by a novel one).

Two identical arenas, 41.5 × 41.5 cm gray plastic box, were placed side by side (one mouse in each arena) and were simultaneously used. The center of the arena was digitally defined as an 8.5 × 8.5 cm square area. Objects were visually and tactilely distinct. To control for potential positional preference, the location of the novel object relative to that of the familiar object was randomized. Mouse behavior was recorded by a camera placed in the room's ceiling, and was subsequently analyzed using Ethovision XT 11 software (Noldus). Novel object preference was scored using the "discrimination index", defined as the time spent exploring the novel object relative to the total exploration time (%) during the test trial. Two mice with total exploration time less than 5 s were excluded from the study. A discrimination index above 50% indicates novelty recognition, with 50% indicating no preference. After each trial, the arenas and equipment were wiped with 10% ethanol. Female and male mice were tested in separate experimental blocks run 1.5 h apart.

Histology and immunohistochemistry

Paraformaldehyde-fixed paraffin-embedded mouse brains and human CP samples were sagittally sectioned with thickness 6 μm. One slide per mouse or human subject was used for staining. After deparaffinization in xylene and rehydration though a degrading series of ethanol solutions, antigen retrieval was performed as specified below (Antigen retrieval section). For human slides, before antigen retrieval, endogenous autofluorescence was quenched with 0.1% Sudan Black B (Sigma) in 70% ethanol for 20 min at room temperature. Sections were blocked with 20% normal donkey serum in PBS with 0.3% Triton X-100 for 1 h at room temperature, and then incubated with primary antibodies diluted in PBS with 2% normal donkey serum and 0.3% Triton X-100 for one overnight at room temperature, followed by one additional overnight at 4°C. For IBA1 staining, anti-IBA1 antibody was applied for one overnight only at room temperature. Primary antibodies used and relative dilutions were: rabbit anti-mouse cleaved caspase 3 (1:100; Cell Signaling, 9661S); rabbit anti-mouse claudin 1 (1:100; ThermoFisher, 51–9000); rabbit anti-mouse/human CYP46A1 (1:50; Proteintech, 12486-1-AP); rabbit anti-GFAP (1:150; Dako, Z0334); rabbit ant-IBA1 (1:150; Wako, 019–19741). After rinsing, sections were incubated with secondary antibodies diluted in PBS (mouse slides) or PBS with 2% normal donkey serum and 0.3% Triton X-100 (human slides) for 1 h at room temperature. Secondary antibodies included: Cy3-conjugated donkey anti-rabbit antibody (1:150; Jackson ImmunoResearch); biotin-SP-conjugated donkey anti-rabbit secondary antibody (for mouse CYP46A1 staining; 1:150; Jackson ImmunoResearch). When biotin-SP-conjugated secondary antibody was used, slides were subsequently incubated with Cy3-conjugated streptavidin (1:150; Jackson ImmunoResearch) in PBS for 15 min. For mouse sections, nuclei were counterstained with Hoechst dye 33342 (1:5,000; Invitrogen) for 1 min. Slides were mounted with Aqua-Poly/Mount (Polysciences). For staining of mouse CP explants, tissue from left lateral ventricles was fixed with 2.5% paraformaldehyde for 30 min at room temperature, after which it was either stained immediately or stored in PBS containing 0.05% sodium azide (Sigma). Tissue was cleared in CUBIC-1 solution[82] (25% urea, 25% quadrol, 15% Triton X-100 in distilled water) for 3 h at room temperature. After rinsing with PBS with 0.3% Triton X-100, tissue was blocked for 1 h at room temperature using the Mouse On Mouse detection kit (Vector labs) according to manufacturer's instructions, and then incubated with primary antibodies diluted in PBS with 8% Mouse On Mouse protein concentrate and 0.3% Triton X-100 for one overnight at 4°C. Primary antibodies used and relative dilutions were: rat anti-mouse CD31 (1:100; BD Biosciences, 553370); rabbit anti-mouse/human CYP46A1 (1:200; Proteintech, 12486-1-AP); mouse anti-mouse ZO-1 (1:100; Invitrogen, 33–9100). After rinsing with PBS with 0.3% Triton X-100, tissue was incubated with secondary antibodies diluted in PBS with 2% normal donkey serum and 0.3% Triton X-100 for 1 h at room temperature. Secondary antibodies included: Cy2/3-conjugated donkey anti-mouse/rabbit antibodies (1:150; Jackson ImmunoResearch). Nuclei were counterstained with Hoechst dye 33342 (1:5,000) for 3 min. Subsequently, tissue was incubated in 1:1 distilled water:CUBIC-2 solution[82] (50% sucrose, 25% urea, 10% triethanolamine, 0.1% Triton X-100) for at least 30 min at room temperature, and then mounted with CUBIC-2 solution. For inspection of green fluorescent protein (GFP) expression in AAV_GFP-injected 5xFAD mice, brains were fixed in 2.5% PFA for 2 overnights followed by addition of 60% sucrose to a final concentration of 30% for an additional 3 overnights. Subsequently, brains were sliced in 30 μm thick coronal sections and preserved in PBS containing 0.05% sodium azide solution. For visualization of the GFP signal, slices were washed and subsequently mounted with Aqua-Poly/Mount (Polysciences).

Antigen retrieval

For Cleaved caspase 3, GFAP, and IBA1 staining on mouse sections, slides were microwave-heated at 100% power to boiling point in 10 mM sodium citrate buffer pH 6.0, 0.05% Tween 20 for 3 min, then 20% power for 8 min, finally cooled on the bench for at least 20 min. For Claudin 1 staining on mouse sections slides were microwave-heated at 100% power to boiling point in 10 mM Tris buffer pH 9.0, 0.05% Tween 20 for 3 min, then 20% power for 20 min, finally cooled on the bench for 30 min. For CYP46A1 staining on mouse sections, slides were microwave-heated at 100% power to boiling point in 10 mM citric acid buffer pH 6.0 for 3 min, then 20% power for 8 min, finally cooled on the bench for 20 min. For CYP46A1 staining on human sections, slides were microwave-heated at 100% power to boiling point in 10 mM sodium citrate buffer pH 6.0, 0.05% Tween 20 for 3 min, then 20% power for 20 min, finally cooled on the bench for 30 min. Note: The same protocol also works with 10 mM Tris buffer pH 9.0, 0.05% Tween 20.

Image processing and quantification

Bidimensional microscopic images of mouse slices were acquired using an epifluorescence microscope (E800; Nikon) equipped with a digital camera (DXM 1200F; Nikon) and using either a 20× NA 0.50, a 40× NA 0.75 or a 4× NA 0.10 objective lens (Plan Fluor; Nikon). Images were taken using the NIS-Elements (F3, Nikon). Microscopic stacks of human slices or mouse CP explants were acquired using a laser-scanning confocal microscope (LSM880; Zeiss) equipped with a 63×/1.4 Oil DIC objective lens. Epifluorescence

microscopy images or sum intensity projections of confocal Z-stacks were processed using segmentation algorithms to mask stained areas and subsequently measuring mean gray value, integrated density, and staining coverage (masked stained area over area of the region of interest, %). For sum intensity projections of confocal Z-stacks, the mean gray value of the stained area was further divided by the stack's depth to obtain the normalized mean gray value. For quantification, the measurements relative to 3-5 sections per mouse CP (slide), 5 fields per human CP (slide), and 4 stacks per mouse CP organ culture were averaged. Representative images were optimized using ImageJ[75] and processed equally for all experimental conditions displayed.

Sample preparation and ELISA for human Aβ1-42

Hippocampi were homogenized 100 mg/mL in TBSE solution (50 mM Tris, 150 mM NaCl, 2 mM EDTA, pH 7.4) with the addition of 1% Protease Inhibitor Cocktail (Sigma Aldrich) using a microtube homogenizer with plastic pestles. The homogenates were centrifuged for 40 min at 350,000 g in 500 μL polycarbonate centrifuge tubes (Beckman Coulter) at 4°C in an Optima MAX-XP Ultracentrifuge with a TLA 120.1 rotor (Beckman Coulter). The supernatant ("TBSE-soluble fraction") was collected, aliquoted, and stored at −80 °C until use. The pellet was resuspended in TBSTx solution (50 mM Tris, 150 mM NaCl, 1% Triton X-100, pH 7.4), using the same volume as for TBSE in the homogenization step. The resuspensions were centrifuged for 40 min at 350,000 g at 4°C and the supernatant ("TBSTx-soluble fraction") was collected, aliquoted, and stored at −80°C until use. BCA assay (Pierce BCA Protein Assay Kit) was performed to determine total protein amount for normalization. To quantify Aβ1-42 peptides, the human Aβ42 Ultrasensitive ELISA Kit (Invitrogen) was used according to the manufacturer's instructions. Data were acquired using a Spark microplate reader (Tecan).

Bulk RNA-seq of primary mouse CP cell cultures

RNA purification and library preparation

Messenger RNA was extracted from primary CP cultures using the Dynabeads mRNA purification kit (Invitrogen). Libraries were prepared using a modified MARS-seq protocol[83] for bulk sequencing. Briefly, mRNA was reverse-transcribed to cDNA, and amplified. cDNA was then fragmented into 300–500 kb fragments, and sample barcode and Illumina adapter sequences were added to each molecule using polymerase chain reaction (PCR).

Low-level processing of the RNA-seq data

MARS-seq libraries, pooled at equimolar concentrations, were sequenced using an Illumina NovaSeq 6,000 sequencer, at a sequencing depth of 1.5 M reads per sample. Reads were condensed into original molecules by counting the same unique molecular identifier (UMI) tags. Mapping of reads was done using HISAT (version 0.1.15)[84]; reads with multiple mapping positions were excluded. Reads were associated with genes if they mapped to an exon, using the UCSC genome browser for reference. Exons of different genes that shared genomic position on the same strand were considered a single gene with a concatenated gene symbol. All downstream analyses were performed in R.

Analysis of RNA-seq data

Bulk sequencing data were analyzed using DESeq2 (version 1.26)[72] and apeglm (version 1.8)[73] packages. All libraries passed quality control, and there were no differences in library size among treatments (mean library size of 10^6 UMIs). Genes with less than 10 total UMIs across all samples were removed from the analysis. Principal component analysis (PCA) showed samples clearly clustered by treatment, correlating to principal component 1 (PC1), explaining 83% of the variability in the data. Five DMSO samples were removed from downstream analysis due to evidence of contamination in the sample. A DESeq2 object was created using the dds() function. The underlying statistical model was fit using the DESeq() function with parameter "fitType" set to "parametric". The shrunken $\log_2$ fold changes were computed using the lfcShrink function with the parameter "type" set to "apeglm". Barplots were drawn using ggplot() from the ggplot2 package (version 3.3.3). For differential gene expression analysis, Wald's test was performed with FDR multiple comparison correction with alpha = 0.100. Enrichment analysis for Gene Ontology terms among the differentially expressed genes was performed using Metascape.[85] The full gene list is provided in Table S2.

Analysis of published CP transcriptome data

UMAP projections

Single-nucleus RNA-seq data of mouse CP[22] were retrieved from GEO: GSE168704 (see also https://singlecell.broadinstitute.org/single_cell/study/SCP1366/choroid-plexus-nucleus-atlas). We isolated data from young (4 months) and aged mice (20 months), downsampled from 68,481 to 24,104 cells (12,052 cells per time point), and then removed the cells with a high ratio of mitochondria (>20%), and low-quality cells (<200 and >5,000 features; remaining cells: 23,592). Gene expression was quantified as $\log_2$(TP10K+1) values as in the original study.[22] Using the Seurat package,[74] we normalized and scaled datasets using the NormalizeData() and ScaleData() functions. Twelve dimensions were used as inputs for the FindNeighbours(), FindClusters() (at 0.5 resolution) and RunUMAP() functions for 2D uniform manifold approximation and projection (UMAP) visualization. Single-nucleus RNA-seq data of postmortem human CP and cortex[3] were retrieved from GEO: GSE159812 (see also https://twc-stanford.shinyapps.io/scrna_brain_covid19/). The data (Seurat object) were already normalized and subjected to removal of low-quality cells by the authors of the original study[3]; data from one patient with influenza were not included (remaining cells: 24,344 for CP and 36,168 for cortex). For Figures 1H–1J, 1L, 1N, and S4B, data from non-infected individuals only were used (remaining cells: 12,352). Gene expression was quantified as the natural log of normalized counts (ln(normalized counts)).

Comparison of CP transcriptome data

For mouse aging, the analyzed dataset was provided by the authors of ref. [25] (see also https://twc-stanford.shinyapps.io/spatiotemporal_brain_map/, "bulk transcriptome", query "Cyp46a1"). For human diseases, the following publicly available datasets were used: GEO: GSE110226 for AD, FTD, and HD[30]; GEO: GSE137619 for PMS[40]; GEO: GSE159812 for COVID[3] (data from one patient with influenza were not included). For the AD, FTD, and HD datasets (gene expression Affymetrix microarray data), the analysis was performed using the Partek Genomics Suite, version 7.19.1125 (https://www.partek.com/partek-genomics-suite/). Probesets were normalized using RMA.[86] For duplicate gene symbols, we considered the most abundant probeset across all samples (average normalized probeset intensity for the AD, FTD and HD datasets). Genes where at least one sample had a normalized probeset intensity value of at least 5 were introduced in the analysis; gender was taken into account as a random factor. The statistical analysis for differential gene expression was performed using ANOVA with contrasts. For the PMS dataset, Ensembl gene identifiers were converted into gene symbols using the ensembl_symbol_converter tool (https://www.biotools.fr/human/ensembl_symbol_converter). We considered only genes for which a gene symbol was available. For genes that had more than one transcript, we summed the counts of transcripts belonging to the same gene, per sample. Genes were filtered to have a baseMean of at least 5. The statistical analysis was performed using DESeq2 (version 1.16.1; ref.[72]); gender was added to the analysis as a factor. For the COVID dataset (single-nucleus RNA-seq), analysis was performed using the FindMarkers() function and the MAST algorithm (version 1.18.0; ref. [87]) of the Seurat package[74] (version 4.2.0) with the following parameters: test.use = 'MAST', logfc.threshold = 0 and latent.vars = c("Sex", "Batch"). To compare mouse and human datasets, the mouse genes symbols were converted to the corresponding human orthologues based on a list downloaded from https://www.informatics.jax.org/homology.shtml on April 19th, 2023. Pathway enrichment analyses were performed using Metascape[85] on May 7th and 8th, 2023. Transcriptional regulatory networks analyses were performed using the TRRUST algorithm.[88] Protein-protein interaction enrichment analysis was performed using the MCODE algorithm.[89] Venn plots were generated using the VennDiagram package 1.7.3.

Sorting of brain CD45$^+$CD11b$^+$ cells

CD45$^+$CD11b$^+$ cells from the left brain hemisphere were sorted using FACSymphony-S6 and FACS DIVA software (BD Biosciences, San Jose, CA). Cells were gated for CD45 (APC, clone 30F-11; eBioscience, 17-0451-82) and CD11b (PE, clone M1/70; eBioscience, 12-0112-83), while excluding debris (FSC-A vs. SSC-A), dead cells (DAPI$^+$), and doublets (FSC-A vs. FSC-H).

QUANTIFICATION AND STATISTICAL ANALYSIS

Data reporting and replication

No statistical method was used to predetermine sample sizes, which were chosen with adequate statistical power based on the literature and past experience. The specific sample sizes and tests used to analyze each set of experiments are indicated in the Figure legends. Investigators were blind to animal identity during experiments and outcome assessment, except during the execution of the NOR assay, where the difference between AAV-injected 5xFAD mice, which underwent surgery, and non-injected WT mice, was obvious. Experimental endpoint was according to IACUC guidelines. For experiments with AAV-injected mice, AAV_mCYP46A1 5xFAD mice were excluded from all analyses assessing the effect of *Cyp46a1* overexpression in the CP if they met the criteria described in the Results, *CYP46A1 overexpression in the CP in 5xFAD mice attenuated brain inflammation* and STAR Methods, *Exclusion criteria for AAV_mCYP46A1 mice*. In addition, animals and samples whose data were of poor quality due to technical failures were also excluded. Statistical parameters (including sample size *n* and what it represents) are mentioned in the Figure legends. For sample sizes n > 3, the Grubbs' test (alpha = 0.050) was used non-iteratively to identify and remove single outliers. For experiments that were repeated at least twice, the resulting data were combined following normalization per experiment; the exact numbers of repetitions are indicated in the Figure legends. For experiments involving primary mouse CP cell cultures, cells dissociated from CP tissue harvested from all ventricles were pooled and subsequently seeded in at least two replicate wells for each condition. Raw and transformed data, statistical analyses including normality testing, null hypothesis testing, simple linear regressions and correlations, and graphs utilized for Figure panels are reported in the Data S1 source data file.

Statistical analyses

Normality of data distribution was evaluated using D'Agostino-Pearson's ("*omnibus* K2") and Shapiro-Wilk's tests and via visual assessment of quantile-quantile plots. For comparing two groups, homogeneity of variance was tested using *F*-test, and means compared using two-tailed Student's *t* test; Welch's correction was applied for heteroscedastic groups. For comparing more than two groups, homogeneity of variance was tested using the Brown-Forsythe's test; for homoscedastic groups, ordinary one-way ANOVA followed by Tukey's *post hoc* test or Dunnett's *post hoc* test was used; for heteroscedastic groups, Brown-Forsythe and Welch's ANOVA tests followed by unpaired Student's *t* test with Welch's correction were used. In case of strong deviations from normality, non-parametric tests were used: two-tailed Mann-Whitney's test for comparing two groups, and Kruskal-Wallis' test followed by Dunn's *post hoc* test for comparing more than two groups. Backward stepwise regression was used to fit CYP46A1 protein signal (mean intensity) in postmortem human CP samples, using age, gender, and disease

status (AD or ND) as independent variables. The statistics summary of the optimal model is reported in Table S1, *Multiple regression statistics*. For pairwise comparisons, $p < 0.100$ was reported in the Figures, rounded to three decimal places; $p < 0.050$ was considered statistically significant. Data analyses were carried out using GraphPad Prism version 9.0, Microsoft Excel, and R. Graphs were generated with GraphPad Prism version 9.0 and R.